



## Submesoscale Cold Filaments in the Gulf Stream

JONATHAN GULA, M. JEROEN MOLEMAKER, AND JAMES C. MCWILLIAMS

*Department of Atmospheric and Oceanic Sciences, University of California, Los Angeles, Los Angeles, California*

(Manuscript received 13 February 2014, in final form 22 May 2014)

### ABSTRACT

A set of realistic, very high-resolution simulations is made for the Gulf Stream region using the oceanic model Regional Oceanic Modeling System (ROMS) to study the life cycle of the intense submesoscale cold filaments that form on the subtropical gyre, interior wall of the Gulf Stream. The surface buoyancy gradients and ageostrophic secondary circulations intensify in response to the mesoscale strain field as predicted by the theory of filamentogenesis. It can be understood in terms of a dual frontogenetic process, along the lines understood for a single front. There is, however, a stronger secondary circulation due to the amplification at the center of a cold filament. Filament dynamics in the presence of a mixed layer are not adequately described by the classical thermal wind balance. The effect of vertical mixing of momentum due to turbulence in the surface layer is of the same order of magnitude as the pressure gradient and Coriolis force and contributes equally to a so-called turbulent thermal wind balance. Filamentogenesis is disrupted by vigorous submesoscale instabilities. The cause of the instability is the lateral shear as energy production by the horizontal Reynolds stress is the primary fluctuation source during the process; this contrasts with the usual baroclinic instability of submesoscale surface fronts. The filaments are lines of strong oceanic surface convergence as illustrated by the release of Lagrangian parcels in the Gulf Stream. Diabatic mixing is strong as parcels move across the filaments and downwell into the pycnocline. The life cycle of a filament is typically a few days in duration, from intensification to quasi stationarity to instability to dissipation.

### 1. Introduction

Elongated buoyancy filaments appear in virtually any high-resolution image of the ocean surface. These structures, visible for instance in ocean color, sea surface temperature (SST), or synthetic aperture radar (SAR), are typically of mesoscale length (30–100 km) and of much smaller submesoscale width (1–10 km or less). Filaments play an important role in oceanic biogeochemistry, affecting both lateral and vertical transport of tracers like nutrients, phytoplankton, and zooplankton larvae (Lehahn et al. 2007).

Submesoscale filaments are known to be produced by the stirring and straining by mesoscale eddies. Their formation and impact for vertical tracer fluxes at the surface have been studied by Lapeyre and Klein (2006) in the surface quasigeostrophic (SQG) framework. The process

of filamentary intensification, or filamentogenesis, at finite Rossby number has been demonstrated theoretically with idealized two-dimensional solutions in McWilliams et al. (2009a), which shows much stronger secondary circulation and intensification rate for cold filaments compared to warm ones. The cause is a horizontal deformation flow that acts on an isolated, favorably aligned filament, causing rapid narrowing and a two-celled secondary circulation with even stronger surface convergence and downwelling at its center than in frontogenesis for a monotonic density gradient (i.e., a conventional front).

The Gulf Stream is full of fronts, filaments, and eddies at meso- and submesoscales. An example of satellite-observed SST of the Gulf Stream flowing along the southeastern coast of the United States is shown in Fig. 1. Both sides of the Gulf Stream exhibit intense fronts in the form of sharp gradients of SST. The wavelike perturbations and warm filaments detrained from the crests of the meanders, clearly visible on the inshore side (also known as the North Wall) of the Gulf Stream, are associated with the propagation of coastal slope eddies. The focus of this paper is the submesoscale cold filaments visible in

---

*Corresponding author address:* Jonathan Gula, Department of Atmospheric and Oceanic Sciences, University of California, Los Angeles, 405 Hilgard Ave., Los Angeles, CA 90095-1567.  
E-mail: gula@atmos.ucla.edu

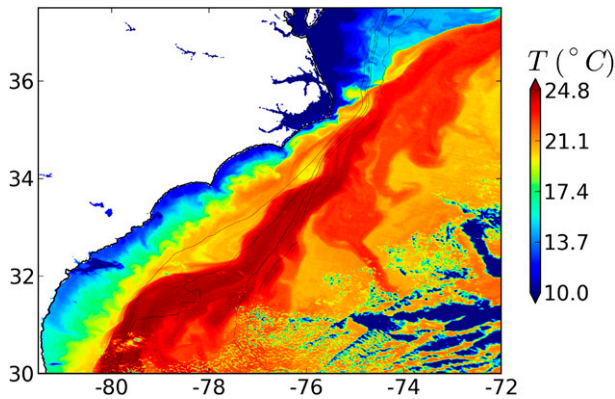


FIG. 1. Observed SST of the Gulf Stream on 31 Jan 2012 (data from Moderate Resolution Imaging Spectroradiometer (MODIS)–*Aqua*). Topography is shown by black isobaths at  $z = -100, -600, -1000,$  and  $-2000$  m.

particular on the South Wall of the Gulf Stream, that is, the open-ocean side within the subtropical gyre, which is a favorable place for the formation of very long and narrow cold filaments due to the intrusion of colder water coming from the open ocean. Multiple cold filaments are seen at various stages of development in Fig. 1. One filament in the process of formation is seen at  $33^{\circ}\text{N}, 76^{\circ}\text{W}$  and another well-formed filament is at  $34^{\circ}\text{N}, 75^{\circ}\text{W}$ , among many other examples. Small cyclonic vortices, in the form of small cold-core surface anomalies, are also spotted regularly close to the East/South Wall of the Gulf Stream. A group of three is visible around  $35^{\circ}\text{N}, 74^{\circ}\text{W}$ , hypothesized to be remnants of a cold filament turned unstable (as shown below in model solutions).

We present and analyze several examples of cold filamentogenesis coming from realistic simulations at very high resolution in the Gulf Stream region. The paper is organized as follows: The simulation setup is presented in section 2. General results from the simulations are described in section 3. The formation of cold filaments in the simulation through the process of filamentogenesis is studied in section 4. In section 5, the momentum balances that characterize a mature cold filament are explored, in particular the impact of the vertical mixing that induces a turbulent thermal wind balance. Mechanisms responsible for the arrest of filamentogenesis are studied in section 6. In section 7, the impact of the filaments on the flow for the transport and mixing of tracers is analyzed in more details. Conclusions of the study are presented and discussed in section 8.

## 2. Simulation setup

The model used in this study is the Regional Oceanic Modeling System (ROMS; Shchepetkin and McWilliams

2005). It solves the hydrostatic primitive equations for the velocity  $\mathbf{u}$ , potential temperature  $\theta$ , and salinity  $S$ , using a full equation of state for seawater (Shchepetkin and McWilliams 2008, 2011). Because our primary target is to expose submesoscale phenomena with horizontal scales of  $O(1)$  km in the vicinity of the Gulf Stream, we use a nesting approach with successive horizontal grid nesting refinements from a parent grid with resolution of  $\Delta x \approx 5$  km covering the North Atlantic Ocean to successive child grids with  $\Delta x \approx 1.5$  km,  $\Delta x \approx 500$  m, and finally  $\Delta x \approx 150$  m. The procedure is offline, one-way nesting from larger to finer scales without feedback from the child grid solution onto the parent grid (Penven et al. 2006). The boundary condition algorithm consists of a modified Flather-type scheme for the barotropic mode (Mason et al. 2010) and Orlanski-type scheme for the baroclinic mode (including  $T$  and  $S$ ; Marchesiello et al. 2001).

Bathymetry for all domains is constructed from the Shuttle Radar Topography Mission (SRTM30 plus) dataset (available online at [http://topex.ucsd.edu/WWW\\_html/srtm30\\_plus.html](http://topex.ucsd.edu/WWW_html/srtm30_plus.html)) based on the 1-min Smith and Sandwell (1997) global dataset and higher-resolution data where available. A Gaussian smoothing kernel with a width of 4 times the topographic grid spacing is used to avoid aliasing whenever the topographic data are available at higher resolution than the computational grid and to ensure the smoothness of the topography at the grid scale. Terrain-following models such as ROMS have computational restrictions with regards to the steepness and roughness of the topography (Beckmann and Haidvogel 1993). Local smoothing is applied where the steepness of the topography exceeds a factor  $r_{\max} = 0.2$ .

Lateral oceanic forcing for the largest domain as well as surface forcing for all simulations are climatological. Simulations are all forced at the surface by a mean monthly climatology of Quick Scatterometer (QuikSCAT) scatterometer winds [Scatterometer Climatology of Ocean Wind (SCOW); Risien and Chelton 2008]. Heat and freshwater atmospheric forcing are from the Comprehensive Ocean–Atmosphere Data Set (COADS; Silva et al. 1994). Freshwater atmospheric forcing has an additional restoring tendency to prevent surface salinity from drifting away from climatological values. This weak restoring is toward climatological monthly surface salinity from the *World Ocean Atlas* (WOA; Conkright et al. 2002). A flux correction term is included in heat atmospheric forcing to allow feedback from the ocean to the atmosphere following the formulation of Barnier et al. (1995). Temperature, salinity, surface elevation, and horizontal velocity initial and boundary information for the largest domain covering the Atlantic ocean are taken from the monthly averaged Simple Ocean Data

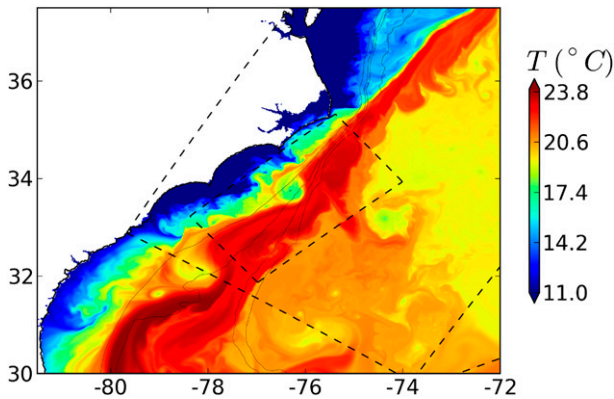


FIG. 2. SST of the Gulf Stream as simulated by ROMS for late winter. The boundaries of the successive nested domains ( $\Delta x = 1.5$  km, 500 m, and 150 m) are delineated by dashed black lines, and within each subdomain SST from the highest resolution is plotted. Topography is as in Fig. 1.

Assimilation (SODA) ocean climatology outputs (Carton and Giese 2008).

The Atlantic domain is an  $800 \times 1200$  grid point orthogonal grid based on an oblique Mercator projection and designed to have nearly uniform spacing in both horizontal directions. This domain is spun up from its initial state for 1 yr, then run for an additional 2 yr. Kinetic energy in the domain is statistically equilibrated within the first few months of simulation. The second and third years of the simulation are used to force the first nested grid covering the Gulf Stream region ( $1000 \times 1600$  grid points with  $\Delta x \approx 1.5$  km). Results obtained after a 6-month spinup are again used to force a second nest ( $1800 \times 1300$  grid points with  $\Delta x \approx 500$  m, partially shown in Fig. 2) covering the region upstream and downstream of Cape Hatteras for about 6 months. Another level of grid refinement yields 4 months of simulation for the domain corresponding to the child grid with the finest resolution ( $1330 \times 2400$  grid points in the horizontal with  $\Delta x \approx 150$  m), which covers the Gulf Stream upstream of Cape Hatteras and is shown in Fig. 2. All domains have 50 levels in the vertical with the same vertical grid system concentrating vertical levels near the surface, following the formula described in Lemarié et al. (2012) with parameters  $h_{\text{cline}} = 300$  m,  $\theta_b = 2$ , and  $\theta_s = 7$ . Finally, vertical mixing of tracers and momentum is done with a  $K$ -profile parameterization (KPP; Large et al. 1994), with the modifications described in Lemarié et al. (2012) based on a bulk Richardson number critical value; here,  $\text{Ri}_{\text{cr}} = 0.45$ .

The goals of the present study are phenomenological discovery, quantification, and dynamical interpretation of cold filaments, not simulation realism per se, although some degree of realism is a necessary condition for

relevance. The most important criterion for the present study is statistical realism of the mesoscale and submesoscale currents in our nested simulations and in our view the model is plausible by these measures. The successive levels of grid refinement spontaneously exhibit an increasingly realistic amount of submesoscale activity (Capet et al. 2008a). Statistics of vertical vorticity, horizontal divergence, and horizontal strain rate for the submesoscale turbulence depicted in the  $\Delta x \approx 500$ -m nest have been validated against observations obtained during the Office of Naval Research (ONR) Lateral Mixing (LatMix) experiment in Shcherbina et al. (2013) in an adjacent region south of the Gulf Stream (i.e., in the submesoscale “soup” away from strong mean currents).

### 3. Filaments in the Gulf Stream

A typical snapshot of SST for late winter from the model is plotted in Fig. 2, showing superimposed results from the three inner domains. The submesoscale cold filaments seen on the surface satellite SST observations on the South Wall of the Gulf Stream (Fig. 1) are well reproduced in the simulations. In both cases, they have similar spatial scales, about 50–100 km long and 1–10 km wide. Our focus here is on the region upstream of the separation of the Gulf Stream at Cape Hatteras, but it should be noted that these filaments occur all along the Gulf Stream, with similar characteristics.

The shallow, warm filaments previously seen on Fig. 1 are also seen in Fig. 2 on the inshore side of the Gulf Stream. These are sometimes known as “shingles” (Lee et al. 1991) and are detached material from the crests of the Gulf Stream meanders due to the presence of slope eddies propagating along the coast. The detached shingles are, however, weakly dynamically active and behave mostly like passive tracers.

The stronger and more dynamically active filaments are the cold cyclonic filaments that are common in observations and numerical simulations. Warm anticyclonic filaments are in general strongly limited by the condition on centrifugal instability ( $\zeta < -f$  with  $\zeta$  the vertical component of vorticity and  $f$  the Coriolis frequency), while there is no such limit on the positive  $\zeta$  values. The upper ocean is known to have a strong positive skewness for  $\zeta$ , that is, favoring cyclonic vorticity structures, in particular filaments (Capet et al. 2008a; Roulet and Klein 2010).

The theory for cross-front density gradient intensification, which has been originally developed in the atmospheric context (Holton 1982) and later applied to the upper ocean (Capet et al. 2008b), involves the sharpening of favorably aligned lateral density gradients by a larger-scale straining flow, disruption of the geostrophic balance for the alongfront flow, and generation

of an ageostrophic secondary circulation. This secondary circulation acts to restore the geostrophic and hydrostatic force balances by advectively tilting isopycnals toward the horizontal, that is, by restratifying the flow. Cold filamentogenesis, as described in [McWilliams et al. \(2009a\)](#), is a related mechanism where the deformation flow acts on a favorably aligned cold filament (a surface density maximum formed by two parallel fronts with opposite sign density gradient), causing an even more rapid narrowing and stronger surface convergence and downwelling at its center than for an isolated front.

Preexisting buoyancy gradients and a mesoscale straining environment are necessary ingredients for frontogenesis and filamentogenesis. Temperature and density gradients, in the form of fronts and filaments, are omnipresent and span all scales of the flow. These structures range from the small fronts and filaments that form the submesoscale soup, barely noticeable in the SST field of [Fig. 2](#), but which stand out in a vorticity or divergence plot (see, e.g., [Shcherbina et al. 2013](#)), to the very intense gradients on both sides of the Gulf Stream and more generally in the vicinity of the larger mesoscale eddies.

Frontogenesis occurs constantly and intense fronts are numerous on both sides of the Gulf Stream. A large number of filamentary structures are seen as well. Long and intense cold filaments, as described previously, are seen preferentially on the South Wall. The mean Gulf Stream velocity structure has a very strong cyclonic shear on the inshore side and a somewhat weaker anticyclonic shear on the open-ocean side, as the velocity cross-stream gradient is amplified at the North Wall. Evidently, the shear is usually too strong and destructive at the North Wall and prevents long cold filaments forming and penetrating into the core of the Stream. On the other hand, the weaker anticyclonic mean shear of the Gulf Stream on its south side is a favorable place for cold cyclonic filaments. Cross-stream fluctuations allow the fronts to intrude into the South Wall and can bring two opposite fronts together by advective pinching to create a cold filament. This asymmetry between the two sides of the Gulf Stream is well illustrated in [Fig. 2](#) downstream from the Gulf Stream separation at Cape Hatteras (around 36°N, 74°W) where several filaments are being formed on the South Wall.

The large amplitudes of velocity and its gradients in the Gulf Stream are likely to generate a very efficient mesoscale straining environment. To distinguish the strain induced by the geostrophic flow from the strain induced by the ageostrophic secondary circulation acting on the fronts or filaments in response to this background straining, the flow is decomposed into a divergent and a nondivergent part. This decomposition is done by

solving a Poisson equation for the divergence of the flow using a multigrid solver with Dirichlet boundary conditions. We get the corresponding nondivergent part of the flow by taking the difference between the total and the divergent part. The nondivergent part of the flow is not formally equal to the geostrophic part but can be considered as a proxy at such scales ([Molemaker et al. 2010](#)). The nondivergent and divergent parts of the flow corresponding to the snapshot of [Fig. 2](#) are plotted as vectors on the right panels of [Fig. 3](#). It shows that the flow is mostly nondivergent. The divergent part of the flow is only significant in the vicinity of intense fronts and filaments in the form of a cross-front convergence. Our interpretation is that the larger-scale nondivergent flow provides the straining environment for the filament, with smaller-scale nondivergent and divergent flows in response. This divergent flow is a good indicator of the ageostrophic secondary circulation generated by frontogenesis at fronts and filamentogenesis at filaments.

The horizontal strain rate is defined as

$$S = \sqrt{(u_x - v_y)^2 + (v_x + u_y)^2}, \quad (1)$$

where  $(u, v)$  are the  $(x, y)$  components of the horizontal flow. The strain induced by the nondivergent ( $S_{\text{rot}}$ ) and divergent ( $S_{\text{div}}$ ) parts of the flow is shown in [Fig. 3](#). The black lines show the direction of the principal strain axis, which is given by the angle  $\theta_p$  such that

$$\tan(2\theta_p) = \frac{v_x + u_y}{u_x - v_y}, \quad (2)$$

and correspond to the direction along which the deformation of the flow is causing the maximum stretching. The principal strain axis is also referred to in meteorology as the dilatation axis ([Holton 1982](#)), and its perpendicular direction is referred to as the contraction axis. The straining will induce frontogenesis if the principal strain axis is aligned with the axis of the front or the filament, that is,  $\theta < \pi/4$ , where  $\theta$  is the angle between the two axis, so that the front or filament is stretched along the frontal direction and gradients are made stronger along the perpendicular direction (axis of maximum contraction). If the angle  $\theta > \pi/4$ , the situation is frontolytic and the straining flow will act to weaken the gradients. Values of the straining rate for the nondivergent flow are large on both sides of the Gulf Stream where we have strong velocity gradients clearly visible in the strain color patterns. We see, however, that the principal strain axis is usually not perfectly aligned with the frontal direction but rotated by an angle slightly smaller than  $\pi/4$ . Gradients of density and velocity on both sides of the Gulf Stream are nearly aligned, and the

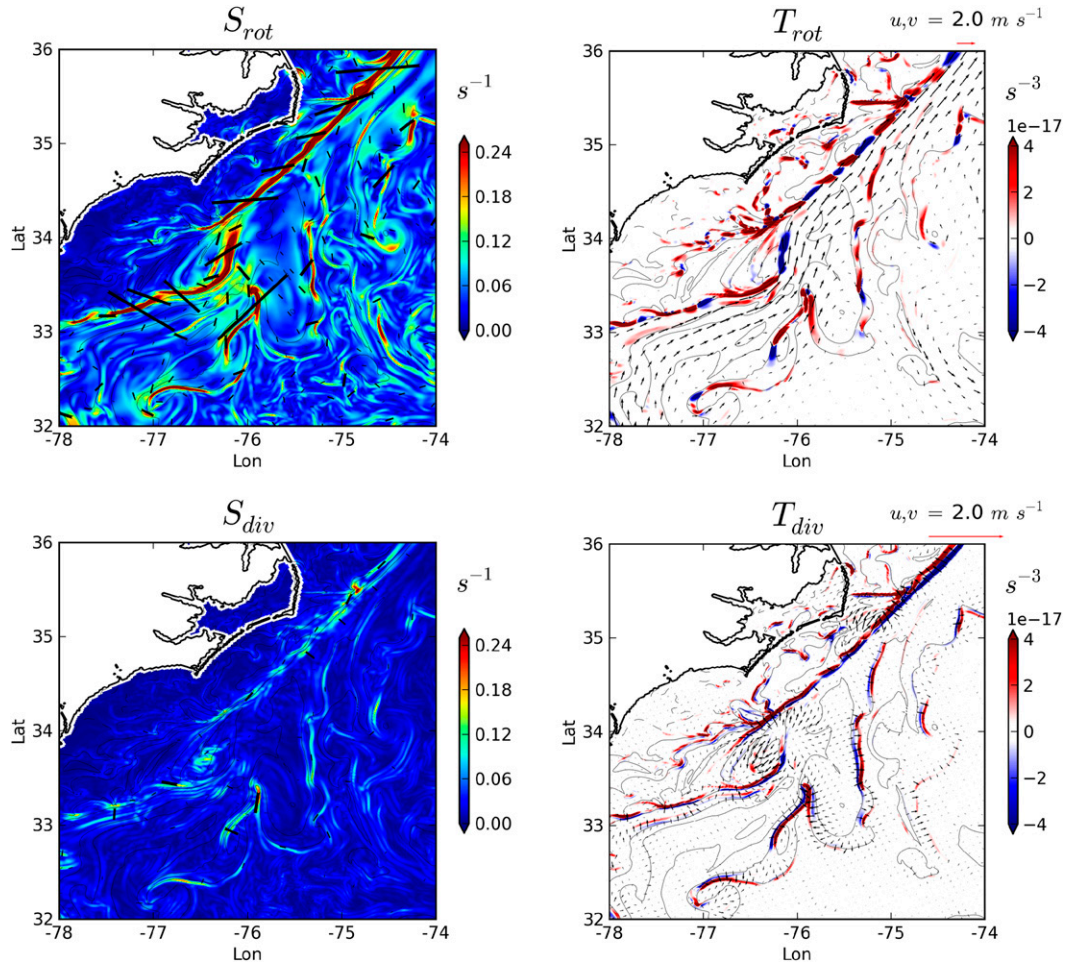


FIG. 3. (left) Instantaneous horizontal patterns of strain  $S$  and (right) frontogenetic tendency  $T$  terms due to the advection by the (top) nondivergent and (bottom) divergent part of the flow at the time and location of Fig. 2 for the 1.5-km resolution nest. Black lines in the left panels indicate the direction of the local principal strain axis and have a length proportional to the amplitude of the strain rate. Black vectors in the right panels show the nondivergent and divergent velocity fields, respectively. Notice that the scale of the arrows for the divergent field has been doubled.

largest contribution to the straining is usually the cross-frontal gradient of alongfront velocity, meaning that the local frontal direction is close to the direction of maximum shear of the flow. The maximum shear direction is given by the angle

$$\tan(2\theta_s) = -\frac{u_x - v_y}{v_x + u_y}, \quad (3)$$

and it is related to the principal strain axis by  $\theta_s = \theta_p \pm \pi/4$ . Values of the strain rate induced by the divergent field (Fig. 3) are a lot weaker than the values of the strain rate induced by the nondivergent field, but as seen from the alignment between fronts and principal strain axis, the straining induced by the divergent field is more efficient at driving frontogenesis as it is mostly a pure cross-front convergent flow.

The condition of alignment of the front or filament with the principal strain axis is strictly equivalent to the condition of a positive frontal tendency due to advection of the horizontal flow. The frontal tendency is the rate of change of the amplitude of the buoyancy gradient following a fluid parcel, defined as in Holton (1982), by

$$T = \frac{1}{2} \frac{D \|\nabla_h b\|^2}{Dt}, \quad (4)$$

where  $b = -g(\rho/\rho_0)$  is the buoyancy,  $\rho$  is the in situ density,  $\rho_0$  is the mean reference density, and  $g$  is the gravitational acceleration.

The frontal tendency  $T$  can be decomposed, following Capet et al. (2008b), into several contributing terms that will be described in section 4. At the mesoscale, we expect the horizontal advection to be the initiating contribution

to the frontogenesis process, and we write the advective frontal tendency as

$$T_{\text{adv}} = \mathbf{Q}_{\text{adv}} \cdot \nabla_h b, \quad (5)$$

where

$$\mathbf{Q}_{\text{adv}} = -b_x \nabla_h u - b_y \nabla_h v, \quad (6)$$

which we can also further decompose into a contribution from the divergent  $T_{\text{adv}}^{\text{div}}$  and the nondivergent  $T_{\text{adv}}^{\text{rot}}$  parts of the flow. Both quantities are plotted in Fig. 3. The regions of strong  $S^{\text{rot}}$  correspond to a positive frontal tendency for fronts and filaments showing that the large-scale straining is the main contributor to the frontogenetic processes. The alternating of regions of positive and negative frontal tendencies is directly related to the meandering of the flow. The frontal tendency induced by the divergent flow has a very distinct pattern with a two-signed signal on each sides of a front or a three-signed signal in the case of a filament. As described in Capet et al. (2008b), the ageostrophic secondary circulation acts asymmetrically to strengthen the front on its heavy side and weaken it on its light side, while the geostrophic flow has a one-signed and uniform contribution consistent with its role in frontal initiation; adapting this to a cold filament, the buoyancy gradients on both sides sharpen.

The filamentary structures that form on the southeast side of the Gulf Stream are where the strongest frontogenesis events happen, leading to the formation of the more intense filaments. The largest values of straining and frontal tendencies (note the amplitude of the black lines on the left panels of Fig. 3) are located at coordinates 33.5°N, 76°W and correspond to the formation of a very strong cold filament. Advective pinching of the South Wall front of the Gulf Stream brings two opposite fronts together to form the filament. We focus in the following on the study of this process of filamentogenesis.

#### 4. Filamentogenesis

The mechanisms involved in filamentogenesis are also active in the frontogenesis of a single front; the buoyancy gradients and velocity shear sharpen at a super-exponential rate in time until limited by an arresting instability and turbulent equilibration or by diffusion (McWilliams et al. 2009a; McWilliams and Molemaker 2011).

We investigate in this section the structure and the dynamics of various cold filaments formed on the South Wall of the Gulf Stream. The bottom panels of Fig. 4 zoom in for four different examples visible on the two upper panels of Fig. 4 and present the finer-resolution

nested domain. They will be designated as  $F_0, F_1, F_2,$  and  $F_3$  hereinafter. These filaments are plotted in Fig. 4 at various stages of their life cycle. The filament  $F_1$  is still in an early stage of the filamentary process;  $F_0$  is more advanced and on the verge of becoming unstable; and  $F_3$  and  $F_4$  are unstable filaments about to break up into small cyclonic vortices.

The entire life cycle of filament  $F_0$  is shown in Fig. 5, which is typical of most of the other filaments in the simulation. Figures 5a–c show a sequence of SST snapshots at intervals of a few hours that illustrates the sharpening temperature gradient and the filamentary intensification of  $F_0$ . Note that unlike in Fig. 4, mean velocities, corresponding to the mean advection of the Gulf Stream (from left to right relative to the figure), have been subtracted from plotted vectors to clearly show the structure of the local differential flow acting on the cold filament. The sharpening of the filament happens very fast; between Figs. 5a and 5c the buoyancy gradient reaches a  $O(1)$  km scale in about 12 h.

A vertical cross section of the filament at the time of Fig. 5c shows the temperature contours and the 3D velocity field in Fig. 6. The vertical structure is typical of a cold filament structure (McWilliams et al. 2009a) with a local outcropping of cold isotherms and a very small lateral width for the temperature and alongfront velocity gradients ( $\Delta L \approx 1$  km). The vectors show the ageostrophic secondary circulation that forms two recirculation cells on each side of the filament. The secondary circulation acts to restore the geostrophic balance by advectively restratifying the flow, that is, tilting the isopycnals toward the horizontal by bringing warm/light fluid from the side toward the center of the filament. The convergence of the flow at the surface gives rise to a very strong and narrow downwelling in the filament middle. Instantaneous values of the vertical velocity can reach  $O(1)$  cm s<sup>-1</sup>.

Figures 7 and 8 show the instantaneous patterns of several frontal quantities at the surface during the filamentogenesis of filaments  $F_0$  (at the time of Fig. 5c) and  $F_1$ . For both filaments, as well as all other equivalent filaments on the South Wall of the Gulf Stream, the background flow acts mostly as a shear flow created by the interactions of larger-scale anticyclonic structures. The angle  $\theta_p$  between the principal strain axis and the filaments [Eq. (2)] is always close to  $\pi/4$ , meaning that the filaments are mostly aligned with the maximum shear direction. The straining field has the same characteristics as the straining field previously shown in Fig. 3 in the lower-resolution nest where the filament  $F_0$  can be seen as the filament being formed at 33.5°N, 76°W. Straining, buoyancy gradient, and frontal tendency are all stronger here due to the higher resolution of the simulation

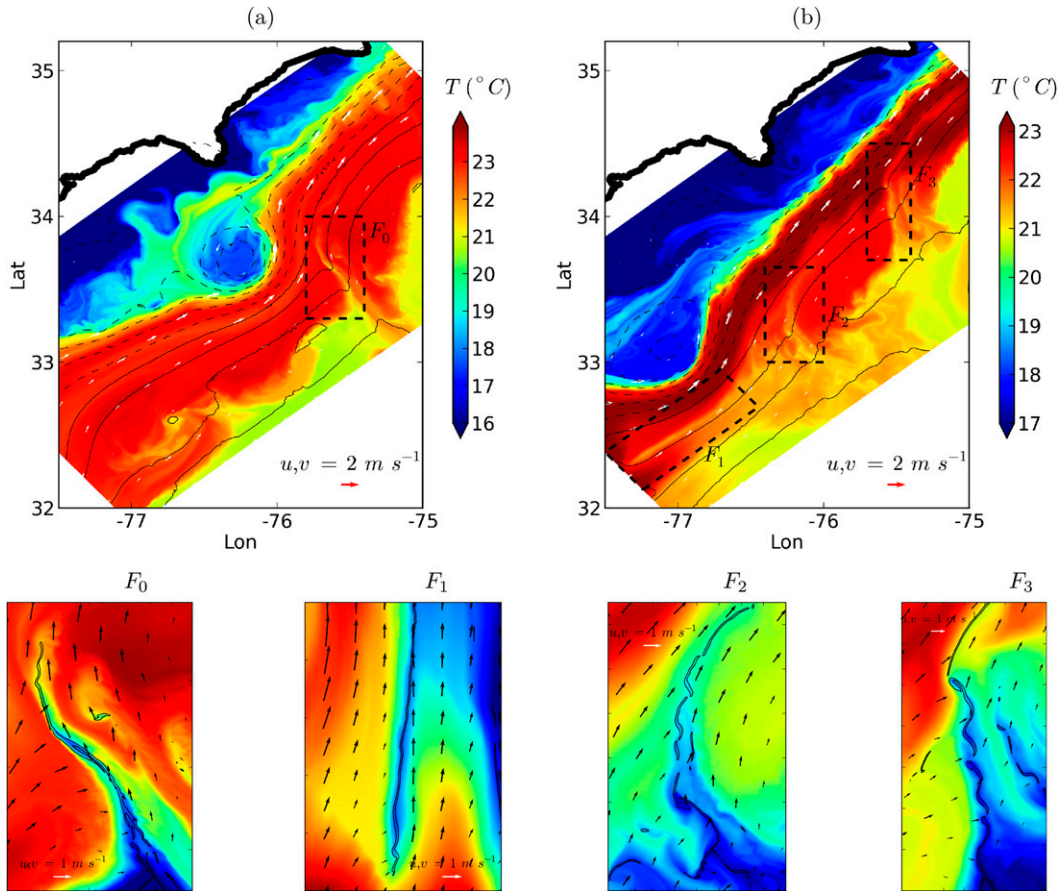


FIG. 4. Simulated SST for a region south of the Gulf Stream separation point at Cape Hatteras on (a) 18 Mar and (b) 13 Mar. Surface velocities are the white vectors. The sea surface dynamic height is shown with thin black contour lines every 0.1 m. Bottom panels show the SST zoomed into the four black rectangles of the two top panels showing submesoscale cold filament intrusions corresponding to the (from left to right)  $F_0$ ,  $F_1$ ,  $F_2$ , and  $F_3$  cases. The color scheme for the bottom panels has been scaled to fit the local SST range. The surface relative vorticity is shown with thin black contour lines, and surface velocity with black arrows.

and the weaker model diffusion. The negative vertical velocity and the corresponding divergence of the flow at the surface generate very strong cyclonic vorticity, up to  $10f$ , through vortex stretching at the center of the filament.

*Frontogenetic diagnosis*

To better understand the mechanisms inducing frontogenesis, we can write the complete frontal tendency equation as in Capet et al. (2008b). In addition to the horizontal advective terms,  $T_{adv} = T_{div} + T_{rot}$ , described previously, there are other terms contributing to the frontal tendency:

$$\frac{1}{2} \frac{D \|\nabla b\|^2}{Dt} = T_{div} + T_{rot} + T_w + T_{dv} + T_{dh}, \quad (7)$$

where

$$T_w = -\frac{\partial b}{\partial z} \nabla_h w \cdot \nabla_h b \quad (8)$$

is the straining deformation by the vertical velocity. It represents the conversion of the vertical buoyancy gradient to horizontal gradient by a component of differential vertical motion in the direction of the existing buoyancy gradient. The rate of frontogenesis related to the diabatic term in the density equation due to the vertical mixing by the KPP scheme is

$$T_{dv} = \nabla_h \left[ \frac{\partial}{\partial z} \left( K_{Tv} \frac{\partial b}{\partial z} \right) \right] \cdot \nabla_h b, \quad (9)$$

where  $K_{Tv}$  is the vertical mixing coefficient for tracers. The effect of horizontal buoyancy diffusion  $\mathcal{D}_h$  is

$$T_{dh} = \nabla_h [\mathcal{D}_h] \cdot \nabla_h b; \quad (10)$$

$\mathcal{D}_h$  in ROMS is implicit in the third-order upwind advection scheme used for momentum and tracers (Shchepetkin and McWilliams 2005). Because an odd-order upwind scheme is approximately equivalent to

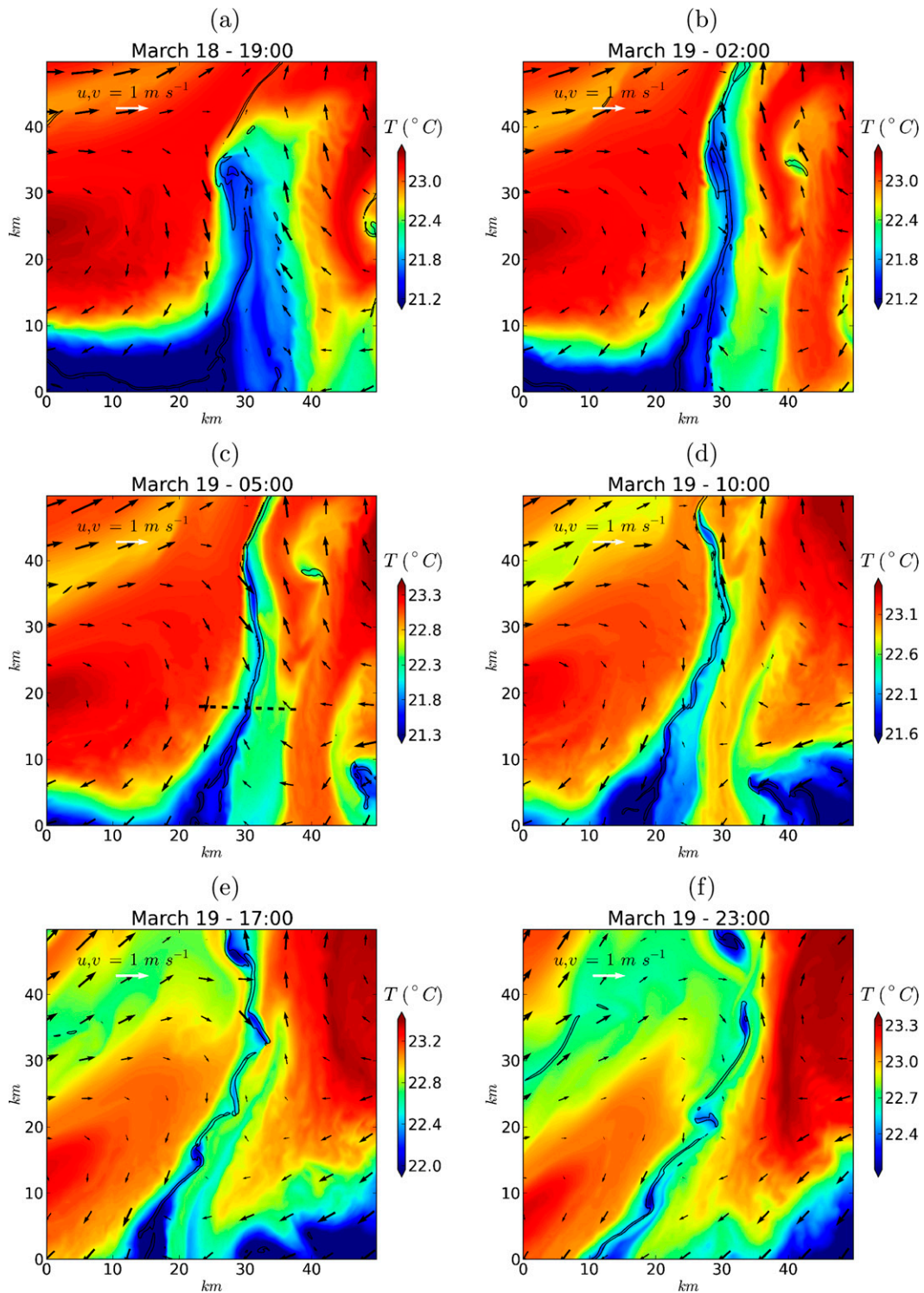


FIG. 5. SST (in colors), surface relative vorticity (black contours), and surface velocity (vectors) for the evolution of the cold filament  $F_0$  shown in Fig. 4. The mean velocity (over the plotted domain) has been subtracted from the plotted vectors. Times indicated are UTC.

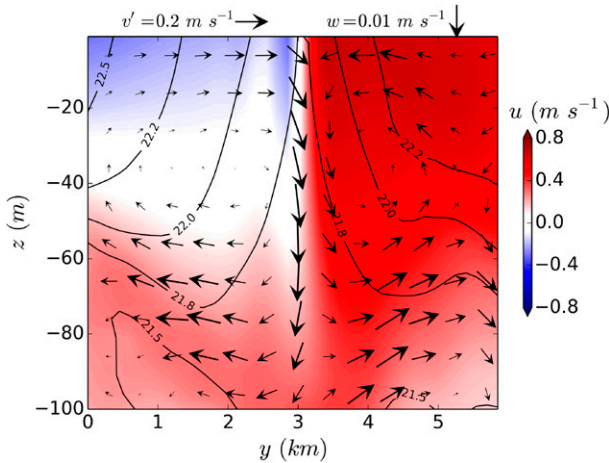


FIG. 6. Vertical section of alongfront velocity (in colors), cross-front and vertical velocities (vectors), and temperature (black contours) along the dashed black line in Fig. 5c.

the next higher-order (even) scheme plus a diffusive term  $\propto \nabla^p$  with  $p$  equal to the higher even order (Holland et al. 1998; Webb et al. 1998), we can estimate the effective horizontal hyperdiffusion acting on the tracer as the difference between the third-order upwind scheme and a fourth-order centered scheme.

The different frontogenetic terms are plotted in Figs. 9 and 10 for filaments  $F_0$  and  $F_1$ , respectively, in the same horizontal planes as in Figs. 7 and 8 at depth  $z = -5$  m. Both filaments are at an advanced phase of their intensification, where gradients are close to their maximum value and the horizontal straining effect is not the only one to play an important role anymore. The horizontal advection  $T_{adv}$  is still the largest contribution with a strong positive signal at the center of the filament from both the nondivergent and the divergent part of the flow. The vertical straining  $T_w$  is negative everywhere, but very small because  $w$  is zero at the surface. The horizontal diffusion  $T_{dh}$  has its primary negative contribution where the velocity shear is maximum; that is, it acts to weaken the front, but in these examples it is not a dominant term. Finally, the vertical mixing  $T_{dv}$  seems to oppose the effect of the advection with a negative signal at the center and positive signals on the exterior sides of the filaments;  $T_{dv}$  is larger than  $T_{dh}$  here.

Vertical sections along the dashed yellow line in Fig. 9 are shown in Fig. 11. Both horizontal advective terms are surface intensified and active only in the upper mixed layer on the sides of the filament. The nondivergent part of advection has an overall positive contribution, while the divergent part is locally more intense but acts more asymmetrically to strengthen the filament in its center while weakening it on its sides. The vertical straining is small at the surface, but becomes larger at depth where

the vertical velocity is maximum; it weakens the buoyancy gradient everywhere. The strong and noisy signals at the bottom of the boundary (marked by a dashed red line) and below are associated with internal gravity waves that are abundant in our model and not filtered out by any kind of averaging.<sup>1</sup> The horizontal diffusion acts to weaken the gradients mostly at the surface, where the velocity shear is maximum, and locally at the bottom of the boundary layer where there is internal wave activity. The vertical mixing contribution  $T_{dv}$  has opposite signs compared to  $T_{div}$  and will act to weaken the filament in its center but reinforce it on the sides. The pattern and signs of the contribution from the different terms to the frontogenetic tendency for each side of the filament taken individually are consistent with the results obtained for isolated fronts (Capet et al. 2008b). However, there is a strong asymmetry in the case of the filament due to the amplification at its center compared to the case of a single front for which the different terms have similar amplitude on each side.

Asymmetries between the two sides of the filament can also be seen in Figs. 9–11. Straining and the subsequent frontogenesis do not act on filaments homogeneously in space as it would for an idealized filament in a symmetric straining flow (McWilliams et al. 2009a).

### 5. Turbulent thermal wind balance in the surface layer

The traditional view for filaments and fronts, as well as most mesoscale currents, assumes that the basic cross-frontal momentum balance is geostrophic, meaning that the cross-front pressure gradient is in balance with the Coriolis force associated with the alongfront velocity. By differentiating vertically the momentum equation and combining with the hydrostatic approximation, we get the well-known thermal wind relation:

$$\begin{aligned}
 -f \frac{\partial v_g}{\partial z} &= -\frac{\partial b}{\partial x} \\
 f \frac{\partial u_g}{\partial z} &= -\frac{\partial b}{\partial y},
 \end{aligned}
 \tag{11}$$

where  $x$ ,  $y$ , and  $u_g$ ,  $v_g$  are the along- and cross-front coordinates and geostrophic velocity components, respectively.

<sup>1</sup> Because of climatological, nontidal forcing as well as insufficient grid resolution, our simulations are deficient in inertia-gravity waves compared to reality. The waves that do arise are spontaneous emissions from the flows that have mostly advective, balanced dynamics. Some fraction of the internal waves near the filaments is due to local emission, although we have not quantified this.

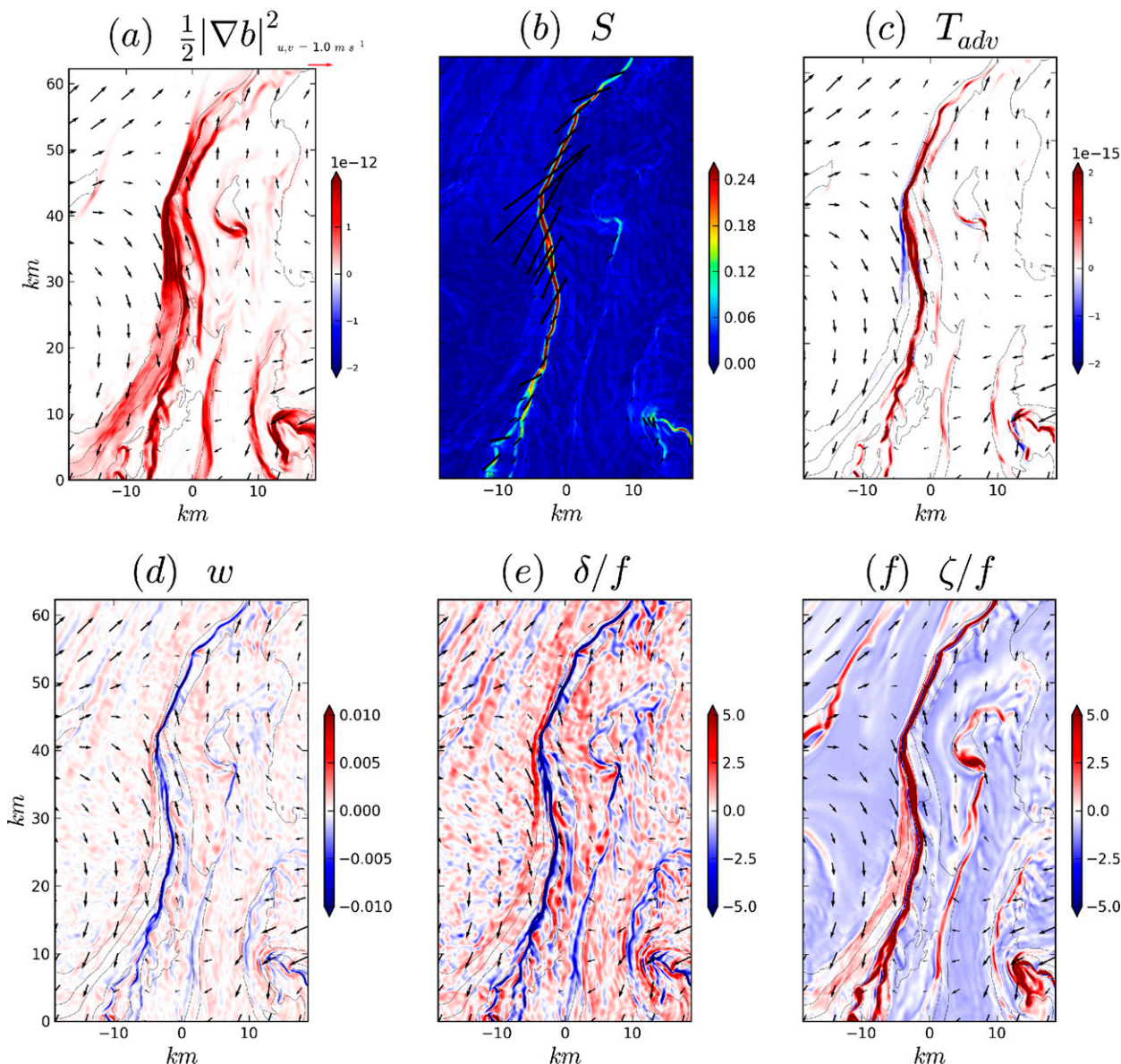


FIG. 7. Instantaneous horizontal patterns at the surface during the intensification of the cold filament  $F_0$  (corresponding in time to Fig. 5c): (a) frontal sharpness  $0.5|\nabla b|^2$ ; (b) strain rate (colors) and principal strain axis (black lines); (c) frontal tendency due to horizontal advection  $T_{adv}$ ; (d) vertical velocity  $w$  (just below the surface); (e) divergence  $u_x + v_y$ , normalized by  $f$ ; and (f) relative vorticity  $v_x - u_y$ , normalized by  $f$ .

The different terms of the thermal wind balance are plotted in Fig. 12 for the filament  $F_1$  during the filamentogenesis process. Differences between Figs. 12a and 12c show that this balance fails in the mixed layer. While the flow is in approximate thermal wind balance in the cross-front direction at the base of the boundary layer, there is a large discrepancy in the upper mixed layer where the cross-front buoyancy gradient is still large, but the vertical gradient of alongfront velocity becomes very small. A more complete picture involves

considering vertical mixing of momentum in both equations such that

$$\begin{aligned}
 -f \frac{\partial v_{ttw}}{\partial z} &= -\frac{\partial b}{\partial x} + \frac{\partial^2}{\partial z^2} \left( K_{Mv} \frac{\partial u_{ttw}}{\partial z} \right) \\
 f \frac{\partial u_{ttw}}{\partial z} &= -\frac{\partial b}{\partial y} + \frac{\partial^2}{\partial z^2} \left( K_{Mv} \frac{\partial v_{ttw}}{\partial z} \right), \quad (12)
 \end{aligned}$$

where  $(u_{ttw}, v_{ttw})$  is the sum of the part of the horizontal flow driven by the momentum mixing and the geostrophic

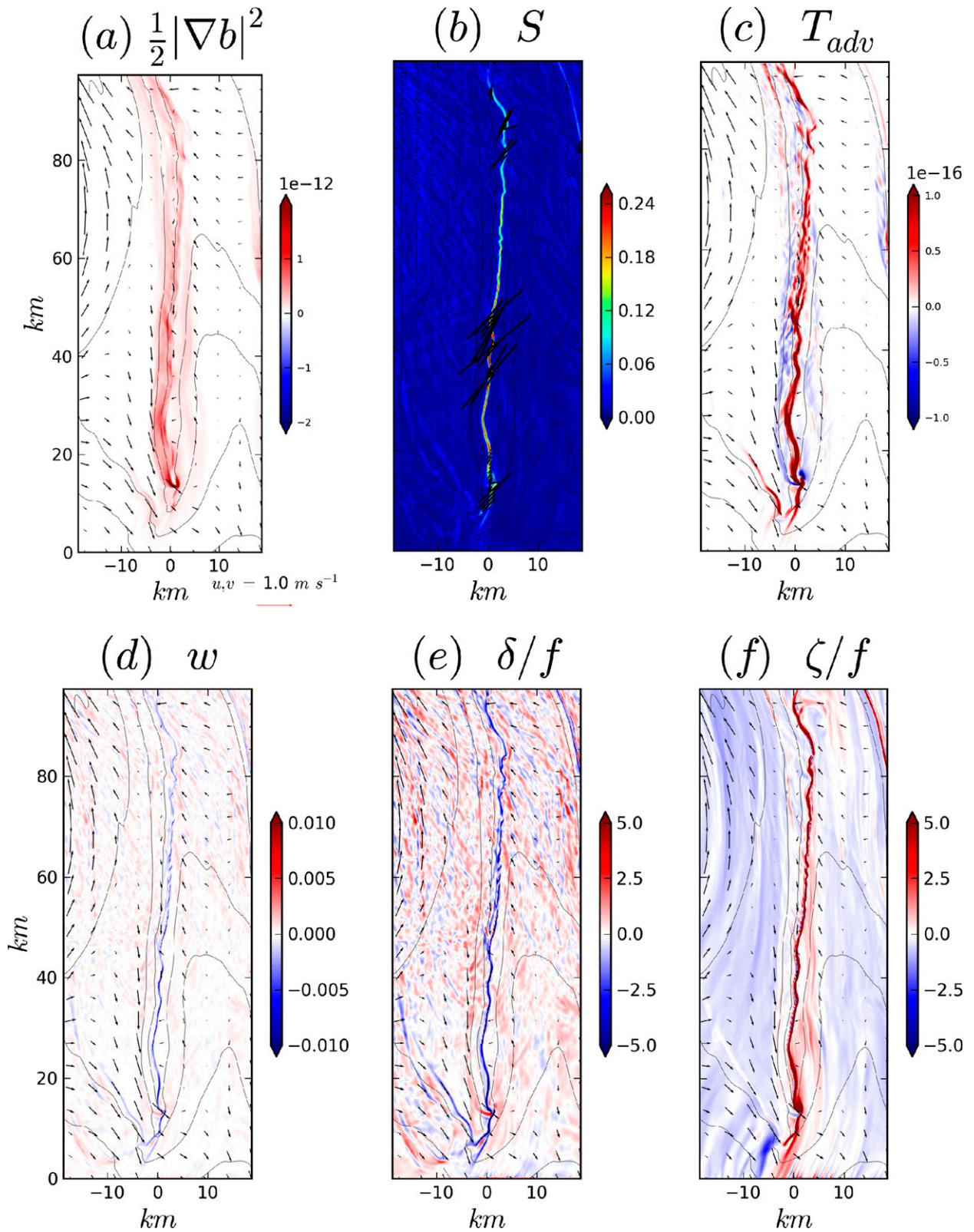


FIG. 8. As in Fig. 7 but for the filamentogenesis of the cold filament  $F_1$ .

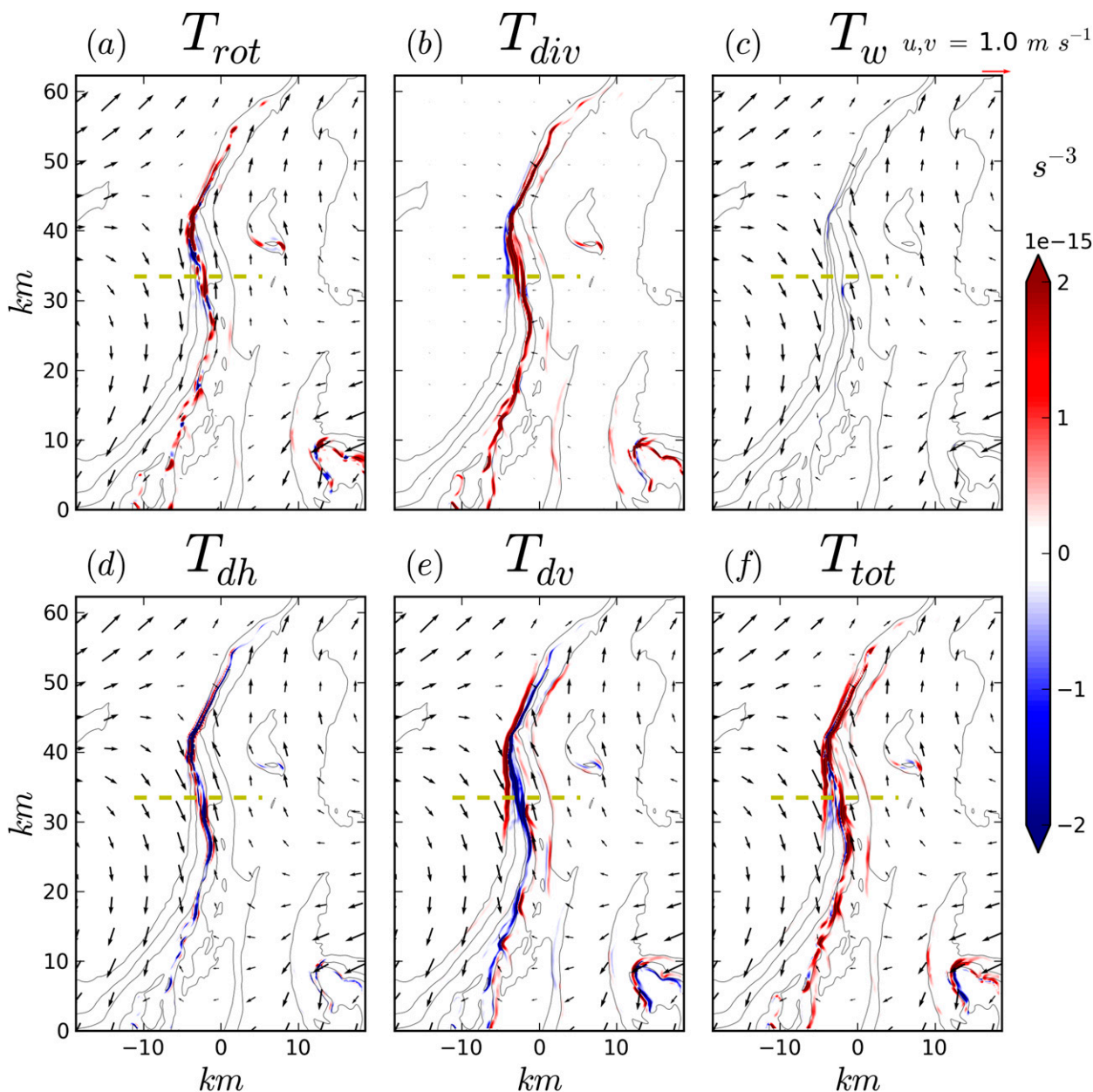


FIG. 9. Instantaneous horizontal patterns of frontogenetic tendency terms for the filament  $F_0$  at  $z = -5$  m at the time of Fig. 5c due to (a) the nondivergent part of the horizontal flow  $T_{rot}$ , (b) the divergent part of the horizontal flow  $T_{div}$ , (c) vertical advection  $T_w$ , (d) horizontal diffusion  $T_{dh}$ , (e) vertical mixing  $T_{dv}$ , and (f) sum of all terms  $T_{tot} = 0.5(D\|\nabla b\|^2/Dt)$ . The vector fields plotted in (a) and (b) correspond to the nondivergent and the divergent parts of the flow, respectively, while the velocity field on the other panels is the total velocity field.

components, and  $K_M(x, y, z)$  is the mixing coefficient for momentum. Equation (12) is a 1D coupled second-order system for  $(\partial u_{tw}/\partial z, \partial v_{tw}/\partial z)$  and describes what can be called a turbulent thermal wind (TTW) balance.

The vertical mixing term (Fig. 12c) is the term balancing the buoyancy gradient in the upper mixed layer. Correspondence between Figs. 12a and 12b shows that the flow is more adequately described by the turbulent

thermal wind balance. There are differences between the two panels, especially below the boundary layer on the positive  $y$  side, which are due to the nonlinear advective terms, including the mean advection as well as fast, small-scale motions as inertia gravity waves, but these on the whole are secondary. In the alongfront direction, there is almost no buoyancy gradient, and the balance is directly between the cross-front flow and the

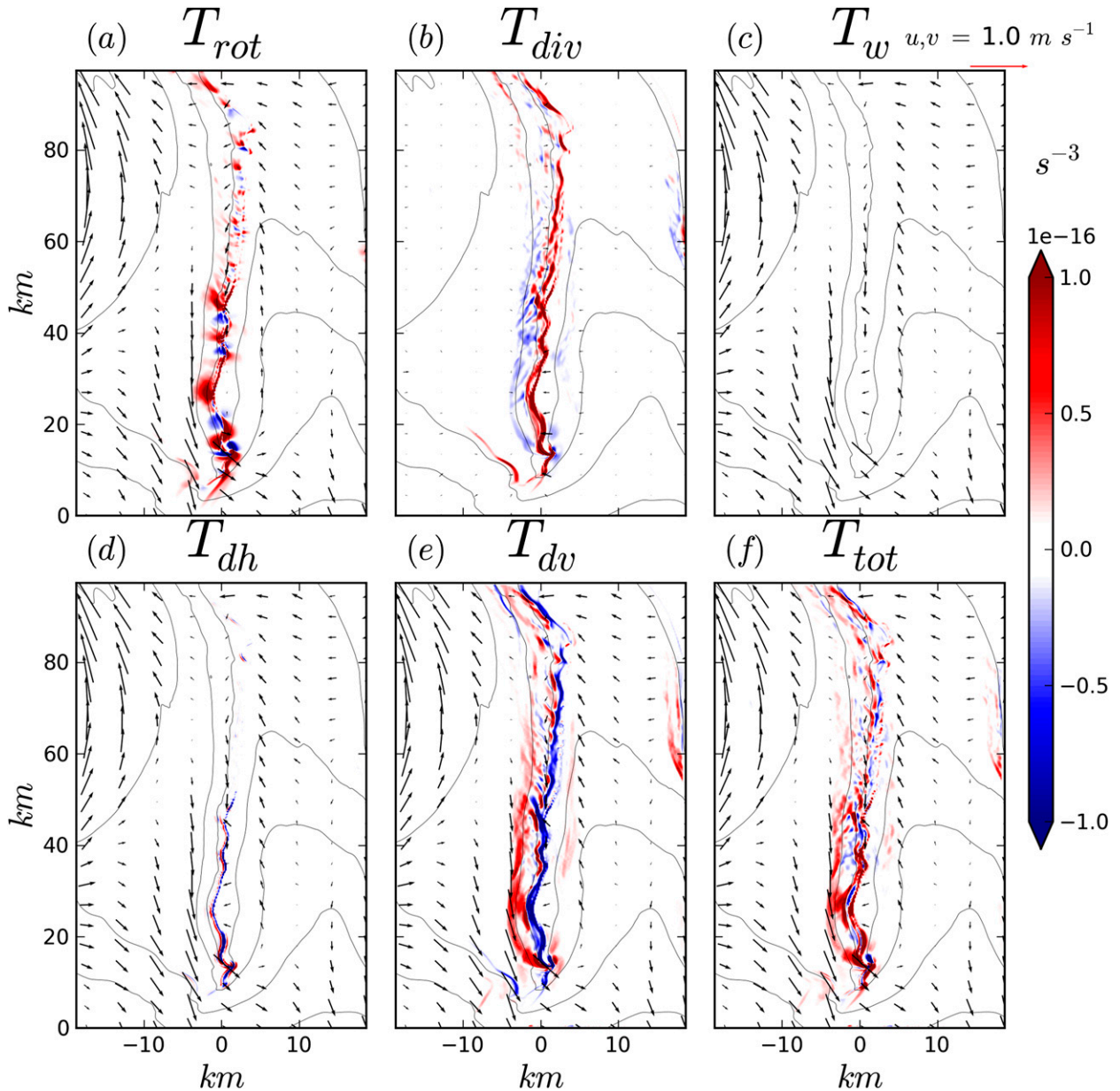


FIG. 10. As in Fig. 9, but for for filament  $F_1$ .

vertical mixing term (not shown). The spatial distribution of the mixing coefficient and the depth of the boundary layer are both highly variable. As seen in Fig. 12, the weaker stratification in the center of the filament corresponds to a larger mixed layer depth and elevated mixing.

Given a buoyancy field, the mixing coefficient for momentum and the surface stress Eq. (12) can be solved directly to obtain the TTW horizontal flow ( $u_{ttw}$ ,  $v_{ttw}$ ). The mixing coefficient is computed by the KPP scheme using the density vertical profiles and the surface forcing (wind stress and buoyancy flux). We solve Eq. (12) for  $(\partial u_{ttw}/\partial z, \partial v_{ttw}/\partial z)$  and then integrate the solution

vertically from the bottom of the ocean to get the TTW associated flow ( $u_{ttw}$ ,  $v_{ttw}$ ). Solving the system at every location gives us the full 3D fields. Boundary conditions at the bottom assume that the flow is close to geostrophic balance in the deep ocean. We do not use a bottom KPP parameterization in the present set of simulations, but it should be noted that in the presence of a bottom boundary layer the boundary conditions would have to be defined outside of it.

Results are shown in Fig. 13 for  $F_1$  at the same time and place as Fig. 12. The geostrophic components give a very good approximation of the flow below the mixed

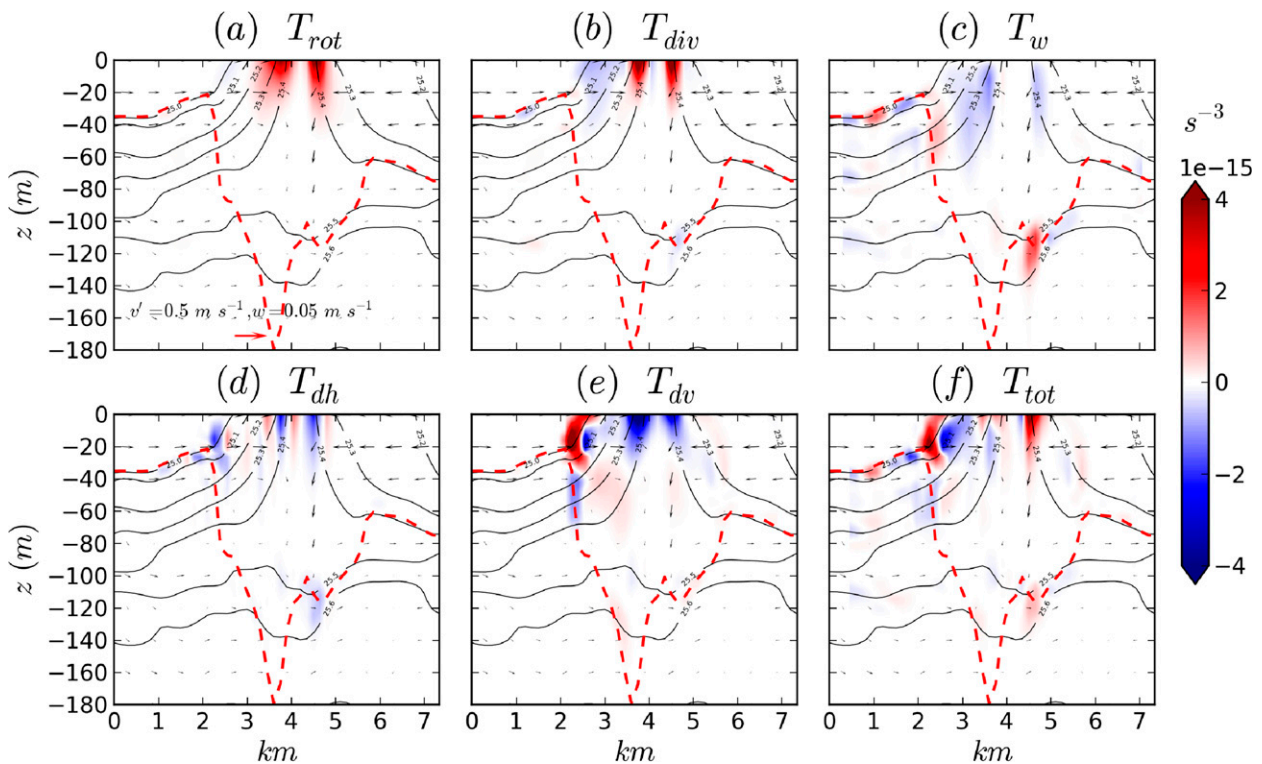


FIG. 11. Instantaneous vertical patterns of frontogenetic tendency terms for the filament  $F_0$  along the vertical section plotted in Fig. 9 due to the (a) nondivergent part of the horizontal flow  $T_{rot}$ , (b) divergent part of the horizontal flow  $T_{div}$ , (c) vertical advection  $T_w$ , (d) horizontal diffusion  $T_{dh}$ , (e) vertical mixing  $T_{dv}$ , and (f) sum of all terms  $T_{tot} = T_{div} + T_{rot} + T_w + T_{dv} + T_{dh}$ . The dashed red line is the base of the boundary layer identified by the KPP scheme.

layer, except for local differences in the form of localized gravity wave signals. As seen in Fig. 12, the cross-front buoyancy gradient, corresponding to the geostrophic vertical shear, is much larger than the vertical velocity shear in the mixed layer. This leads to much larger amplitudes for the geostrophic alongfront velocity  $u_g$  at the surface compared to the real velocity  $u$ . The TTW associated alongfront velocity  $u_{ttw}$  compensates these effects and gives a much more accurate estimate of the real velocity. The cross-frontal circulation in the mixed layer is mostly driven by vertical mixing as there is no buoyancy gradient in the alongfront direction. The cross-front velocity, which corresponds to the ageostrophic secondary circulation of the filament, is well described by the TTW horizontal velocity  $v_{ttw}$ .

The associated vertical velocity  $w_{ttw}$  is computed by integrating the continuity equation from bottom to top. The total vertical velocity and the vertical velocity computed from the TTW associated flow are shown in Fig. 14 for  $F_1$ . As seen from both horizontal and vertical sections, most of the strong negative vertical velocity signal at the center of the filament is described by TTW balance.

Taking into account the role of momentum mixing in frontal dynamics, Garrett and Loder (1981, hereinafter

GL81) state that, considering the small pressure gradient in the alongfront direction, the cross-front flow is mostly balanced by the vertical mixing of momentum, and the mixing-induced cross-front flow can be computed as  $fv_{GL81} = -(K_{Mv}b_y)_z u$ , where  $y$  is the cross-front coordinate. This leads to a momentum-induced vertical velocity  $w_{GL81} = (K_{Mv}b_y)_y / f^2$ . Following these steps, Ponte et al. (2013) computed the diabatic contribution to vertical velocity as  $w_{GL81} = \nabla_h (K_{Mv} \nabla_h b) / f^2$ . This formulation is derived using the fact that the cross-front pressure gradient is in geostrophic balance with the alongfront Coriolis term and is valid only at a small Rossby number, which is obviously not the case for intense fronts or filaments as the ones analyzed here (see Fig. 12). The terms  $(u_{GL81}, v_{GL81})$  are solutions of Eq. (12) if  $(u_{ttw}, v_{ttw})$  are replaced by  $(u_g, v_g)$  in the rhs, that is, only the vertical mixing due to the vertical variations of the geostrophic component of the flow is considered. Computation of  $(u_{GL81}, v_{GL81})$  and  $w_{GL81}$  using our model's  $K_{Mv}$  are shown in Fig. 14. This leads to a serious overestimation of horizontal and vertical velocities in the upper part of the mixed layer compared to the total velocities or to  $(u_{ttw}, v_{ttw}, w_{ttw})$ .

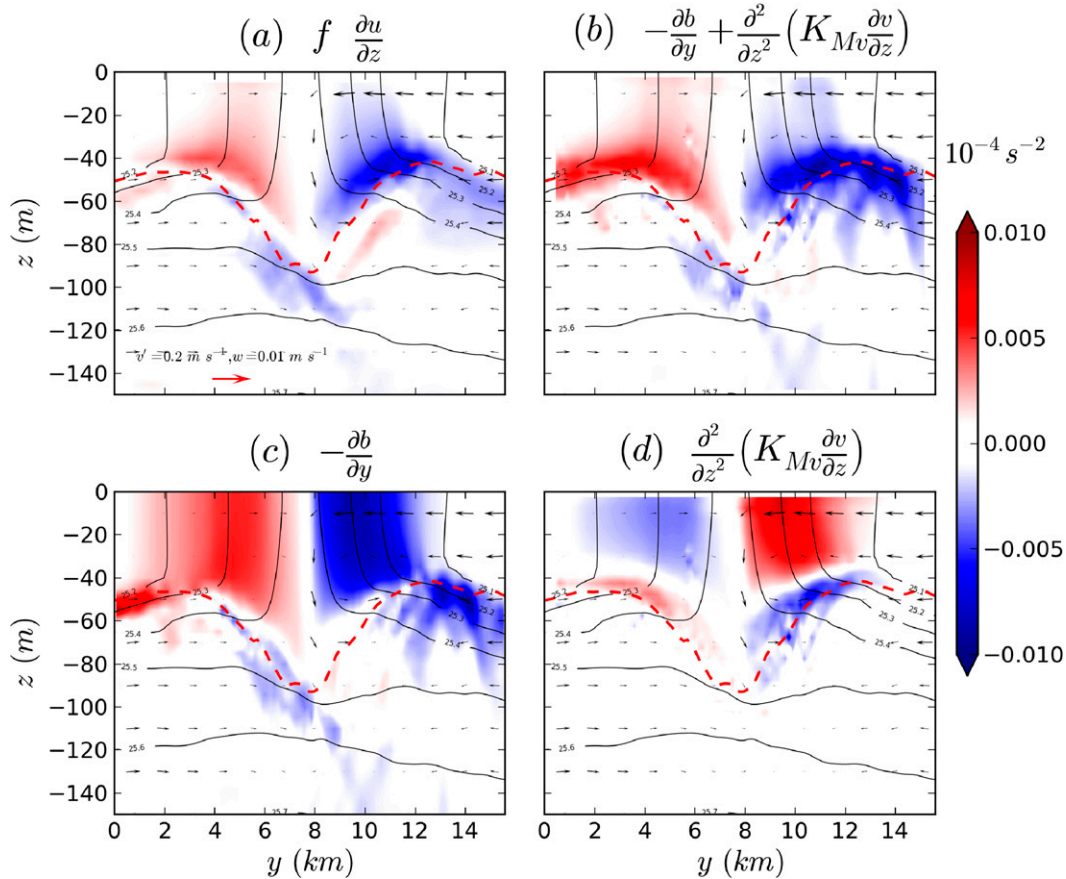


FIG. 12. Vertical sections of the different terms of the turbulent thermal wind balance for the filament  $F_1$  in the cross-front direction  $y$ : (a)  $f \frac{\partial u}{\partial z}$ ; (b)  $-\frac{\partial b}{\partial y} + \frac{\partial^2}{\partial z^2} [K_{Mv} \frac{\partial v}{\partial z}]$ ; (c)  $-\frac{\partial b}{\partial y}$ ; and (d)  $\frac{\partial^2}{\partial z^2} [K_{Mv} \frac{\partial v}{\partial z}]$ . Density is shown in black with a contour interval  $0.1 \text{ kg m}^{-3}$ . All quantities are averaged in the alongfront direction. The dashed red line shows the depth of the boundary layer from the KPP scheme.

In [Ponte et al. \(2013\)](#), the diabatic contribution to vertical velocity is computed using a constant value of  $K_{Mv} = 4 \times 10^{-2} \text{ m}^2 \text{ s}^{-1}$ . It is typical of the values computed here away from intense frontal or filamentary structures, where they locally can reach values of  $K_{Mv} \approx 0.1 \text{ m}^2 \text{ s}^{-1}$ . Despite the underestimation of the mixing coefficient, the lower resolution, and the smaller Rossby numbers, the vertical velocities obtained by this estimation already appear too strong compared to the total velocity field in the vicinity of fronts or filaments [see Fig. 8 in [Ponte et al. \(2013\)](#)]. [Mahadevan and Tandon \(2006\)](#) also investigate the role of the mixing effect in generating vertical motions at ocean fronts using the formulation from [Garrett and Loder \(1981\)](#) but find on the contrary vertical velocity estimates quite lower than observed in the model. This is because their numerical model did not include a boundary layer parameterization, and their vertical velocity estimates were computed using a small and constant background value of  $K_{Mv} = 10^{-5} \text{ m}^2 \text{ s}^{-1}$ .

The TTW balance provides a reliable estimate of the vertical velocity even in cases with such extreme Rossby numbers and horizontal density gradients as the ones presented here. Comparable estimates in lower-resolution simulations (from 500 m to 5 km) show an even better agreement as the unbalanced ageostrophic part of the flow (e.g., gravity waves) is naturally damped in coarser-resolution simulations and for larger-scale dynamical structures. Thus, after an initial intensification of the Gulf Stream cold filaments by the ambient strain field, a quasi-stationary phase can ensue if the strain abates, where the secondary circulation is due to TTW.

## 6. Filamentary arrest

The theory of frontogenesis or filamentogenesis does not explain how it will ultimately be arrested or destroyed. Mechanisms responsible for arrest might be the disappearance of the ambient strain triggering the frontogenesis in the first place, a negative tendency due to the

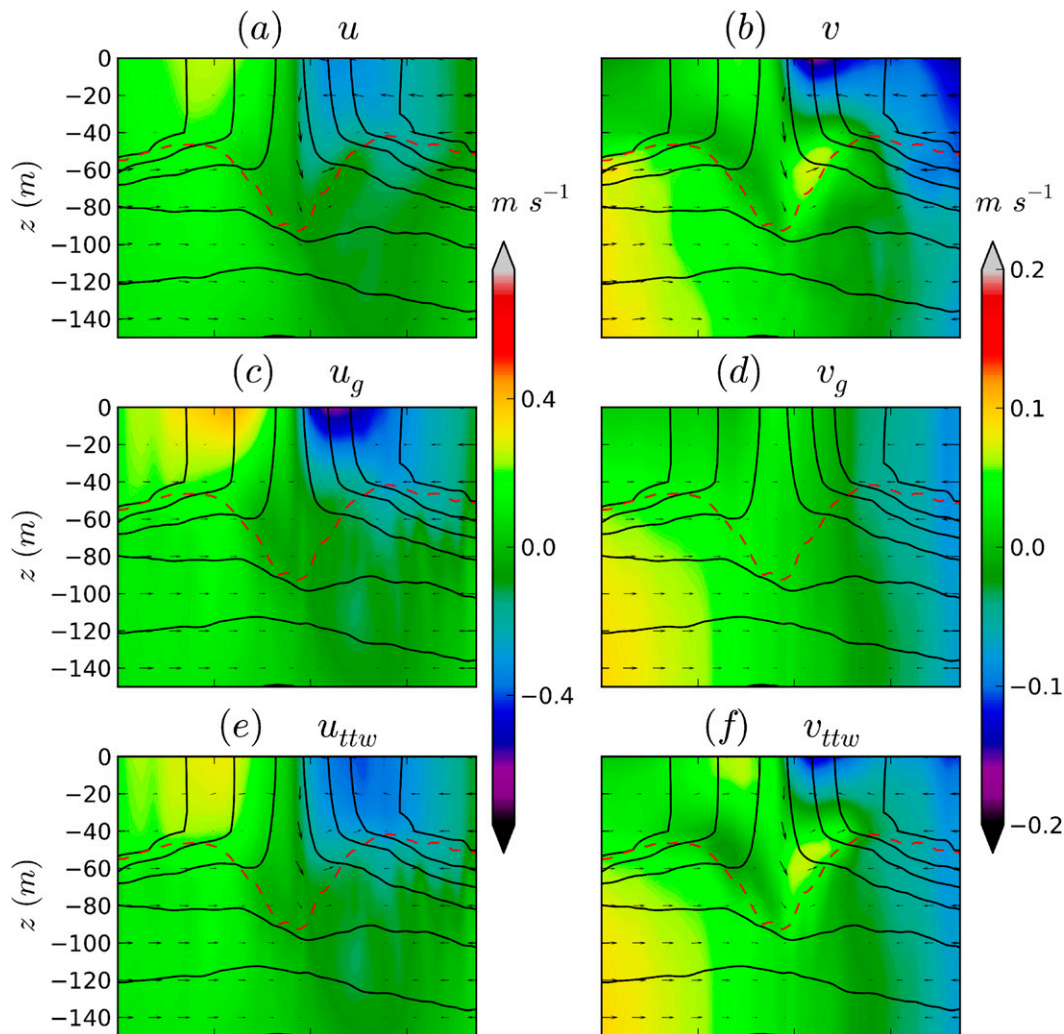


FIG. 13. Vertical sections of (left) alongfront velocity  $u$  and (right) cross-front velocity  $v$  for the filament  $F_1$  in the cross-front direction  $y$ . (a),(b) Total horizontal velocity ( $u, v$ ) from the model, (c),(d) geostrophic components of the horizontal flow ( $u_g, v_g$ ), and (e),(f) TTW associated flow ( $u_{ttw}, v_{ttw}$ ). Density is shown in black with a contour interval  $0.1 \text{ kg m}^{-3}$ . All quantities are averaged in the alongfront direction. The dashed red line shows the depth of the boundary layer from the KPP scheme.

vertical mixing, dissipation by horizontal diffusion, or an instability and eddy feedback equilibration process. McWilliams and Molemaker (2011) show in a quasi-linear model that baroclinic instability during frontogenesis leads to frontal arrest by an eddy buoyancy flux feedback.

Disappearance of the ambient strain is sometimes a controlling factor in our examples. While frontogenesis and the ageostrophic secondary circulation are initiated by the straining of the large-scale flow, it is latter sustained primarily by the TTW balance (section 5). Frontal arrest by the horizontal diffusion will obviously depend on the diffusivity coefficient of the model. It is not unusual for cold filaments in our simulations to reach

lateral scale of  $\approx 1 \text{ km}$ . In the parent ROMS simulations with resolution  $\Delta x \approx 1.5 \text{ km}$  (Fig. 2), cold filaments are damped by the horizontal diffusion when the filament scale comes close to the grid scale. In the smaller domain with  $\Delta x \approx 150 \text{ m}$ , the filaments evolve differently and are arrested on a scale larger than the grid scale. In most cases the sharpening of the filament is disrupted by fluctuations growing and breaking the alongfront regularity of the filament. These perturbations have wavelengths on the order of 5–10 km for the cold filaments in Fig. 4. A sequence of SST snapshots for filament  $F_0$  shows the growth of these fluctuations following the filamentogenesis (Figs. 5d–f). Notice that the whole sequence happens in less than a day. This evolution is

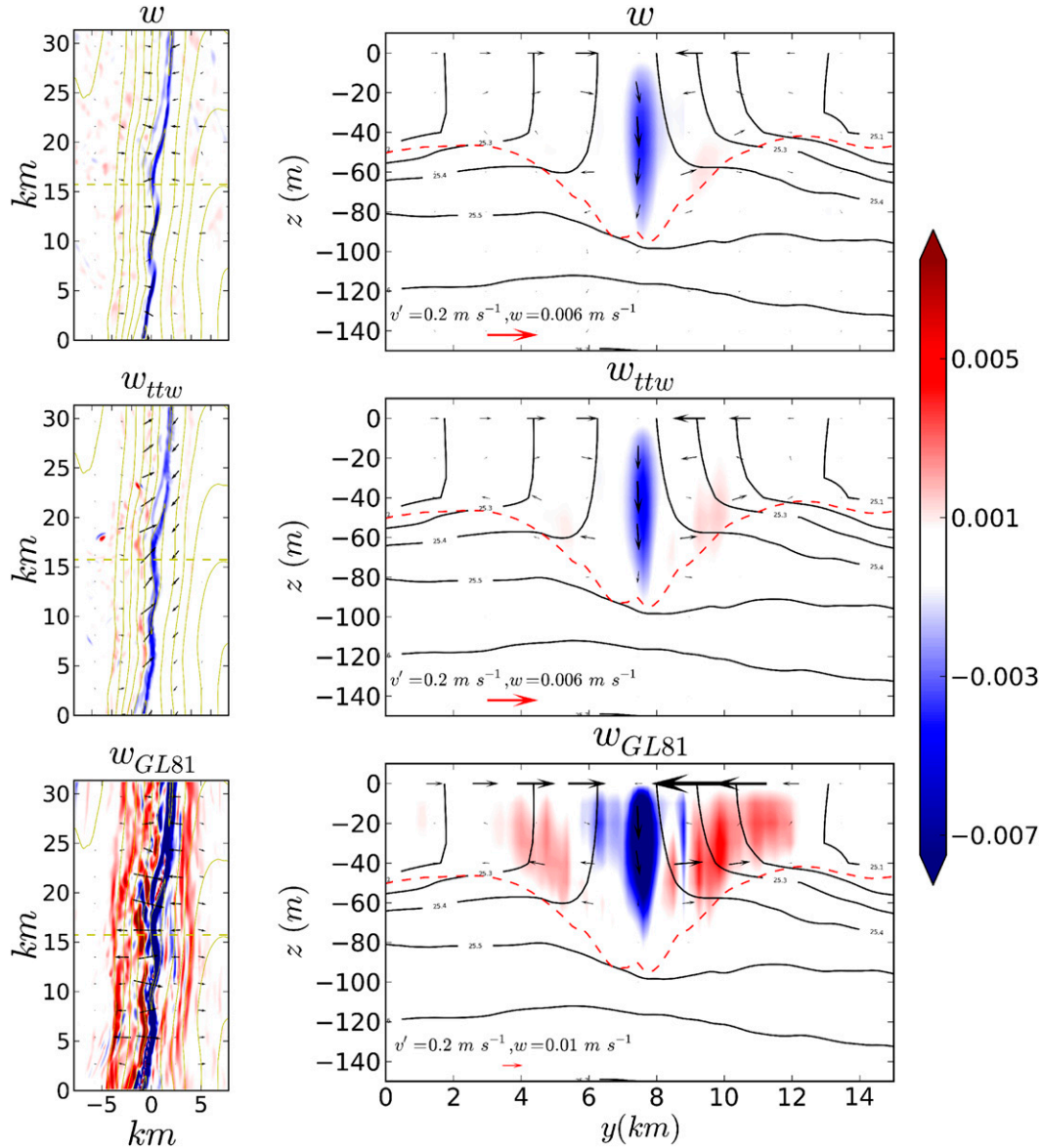


FIG. 14. (left) Instantaneous horizontal patterns of (top)  $w$ , (middle)  $w_{ttw}$ , and (bottom)  $w_{GL81} = \nabla(K_{Mv}\nabla b)/f^2$  for the filament  $F_1$  at  $z = -20$  m. Vectors show the horizontal velocity field: (top)  $(u_{div}, v_{div})$ , (middle)  $(u_{ttw} - u_g, v_{ttw} - v_g)$ , and (bottom)  $(u_{GL81}, v_{GL81})$ . (right) Vertical sections of (top)  $w$ , (middle)  $w_{ttw}$ , and (bottom)  $w_{GL81}$  for the filament  $F_1$  in the cross-front direction  $y$ . All quantities are averaged in the alongfront direction. Vectors show the cross-section velocity field: (top)  $(u_{div}, w_{div})$ , (middle)  $(v_{ttw} - v_g, w_{ttw})$ , and (bottom)  $(v_{GL81}, w_{GL81})$ . Density is shown in green and black contours. The dashed red line shows the depth of the boundary layer from the KPP scheme.

similar for all examples of filaments analyzed in our simulations. The filaments ultimately fragment into a train of submesoscale vortices as a result of the instability process. The signature of these vortices is shown in Fig. 15 for filament  $F_1$  using the difference between absolute vorticity and strain,  $A - S = (f + \zeta) - S$ , and the Okubo–Weiss parameter,  $S^2 - \zeta^2$ . Negative regions in  $A - S$  show that loss of diagnostic force balance is occurring in the vicinity of the filament (McWilliams et al. 1998), while positive

regions in  $S^2 - \zeta^2$  indicate further tracer gradient growth and separation of neighboring trajectories. Loss of balance is consistent with the internal gravity waves evident in the simulation and the large values of both vorticity and divergence compared to  $f$  (Figs. 7–8). In the absence of tides and high-frequency winds that are the usual main sources of internal gravity waves, spontaneous emission (Plougonven and Snyder 2007) is a likely source for the energetic wave field observed in the simulation. The

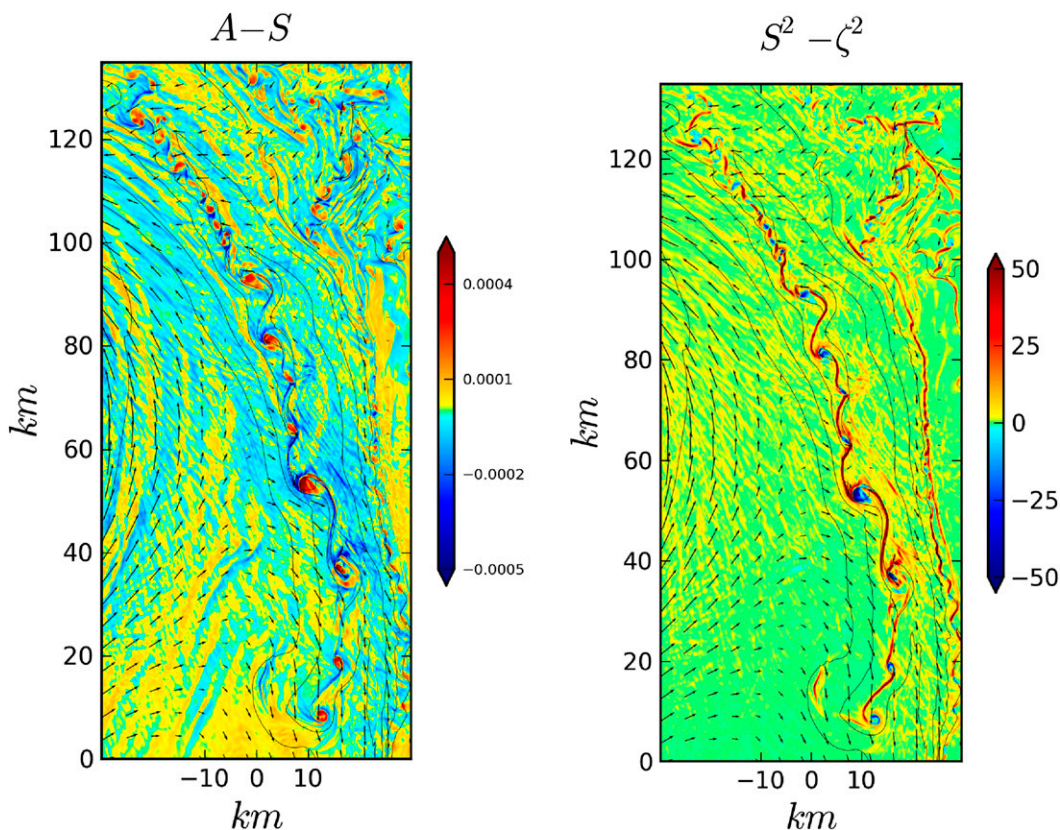


FIG. 15. Instantaneous horizontal patterns at the surface of (a)  $A - S$  and (b) the Okubo–Weiss parameter  $S^2 - \zeta^2$  normalized by  $f^2$  for the filament  $F_1$  that has become unstable. The time of the figure is 30 h later than Fig. 14.

small vortices have strong signatures in both  $A - S$  and  $S^2 - \zeta^2$ , clearly visible as red and blue circles, respectively, with a diameter  $d \approx 3 - 5$  km, indicating that they are balanced and coherent. Instability of the numerous cold filaments in our simulations is responsible for a large number of submesoscale cyclonic vortices at the surface. Thus, the primary filamentary arrest mechanism is a submesoscale instability whose eddy feedback is so strong as to destroy the filament by fragmentation.

*a. Submesoscale filament instability*

To investigate the nature of the submesoscale instability, we compute the kinetic energy conversion terms between the parallel flow along the filament axis and its meandering perturbations in a local reference frame aligned with the filament. The local coordinates are  $x$  and  $y$  in the along- and cross-front direction, respectively, with corresponding horizontal velocities  $u$  and  $v$ . For this analysis the local mean, denoted by an overbar, is defined as the alongfront average for the region considered. We also remove the alongfront trends from the perturbations. Assuming that the local regions considered are of sufficient extent in the  $x^*$

direction to contain a few wavelengths of the frontal instability, any nonzero alongfront trend is part of the background mesoscale flow. Perturbations relative to that mean are denoted with a prime such that the total field can be written  $u = \bar{u} + u'$  and so on. We write energy conversion from mean to perturbation kinetic energy as

$$K_m K_e = \text{HRS} + \text{VRS}, \tag{13}$$

where

$$\text{HRS} = -\overline{u'^2} \frac{\partial \bar{u}}{\partial x} - \overline{u'v'} \frac{\partial \bar{u}}{\partial y} - \overline{v'^2} \frac{\partial \bar{v}}{\partial y} - \overline{u'v'} \frac{\partial \bar{v}}{\partial x} \tag{14}$$

corresponds to the product of horizontal mean shear and Reynolds stress, and

$$\text{VRS} = -\overline{u'w'} \frac{\partial \bar{u}}{\partial z} - \overline{v'w'} \frac{\partial \bar{v}}{\partial z} \tag{15}$$

arises from vertical shear of the mean flow and vertical Reynolds stress. The eddy potential to eddy kinetic energy conversion is

$$P_e K_e = \overline{w'b'}, \quad (16)$$

where  $b$  is the buoyancy anomaly relative to the local area average. The mean potential to mean kinetic energy conversion is

$$P_m K_m = \overline{wb}. \quad (17)$$

This term is an indication of the secondary circulation and kinetic energy source for the mean flow (i.e., the filament).

We compute the different terms and show a vertical integral (over the first 200 m) averaged along the front for different cold filament examples in Fig. 16. The  $P_m K_m$  and HRS terms are both important terms at this time. Other sources like the baroclinic term  $P_e K_e$  and vertical shear VRS are negligible here. While  $P_m K_m$  is the dominant term by an order of magnitude or more during the earlier stages of filamentogenesis prior to the onset of instability (corresponding to Figs. 5a,b for filament  $F_0$ ), the HRS term is quickly growing and matching the amplitude of the  $P_m K_m$  term at the early stages of the instability (corresponding to Figs. 5c,d for filament  $F_0$ ) as seen in Fig. 16. The  $P_m K_m$  term is decreasing rapidly after this time, showing that the filamentogenesis process has stopped and the secondary circulation is henceforth weakening. The energy source for the perturbations is the horizontal shear of the mean flow. Horizontal shear instability is the reason for the arrest of the filamentogenesis. The horizontal shear instability process is qualitatively similar to its SQG equivalent and leads to a similar breaking of the filament into a string of vortices (Held et al. 1995; Jukes 1995). The horizontal shear instability can be interpreted as an interaction of two counterpropagating waves on both buoyancy gradients of the filament as can be seen in Fig. 16, in particular Fig. 16e.

The presence of a large-scale strain stabilizes the horizontal shear instability of vorticity filaments in a barotropic flow (Dritschel et al. 1991). But in our case, as for the SQG temperature filaments (Held et al. 1995), the background scale acting to stabilize the flow is at the same time acting to sharpen it and thus increasing the growth rates of the perturbations. (The same is true for a sharpening front; McWilliams et al. 2009b.) Filaments can be stabilized only for a finite time until they thin to a critical width (Harvey and Ambaum 2010). The vorticity of the filaments is too large compared to the background straining to meet any inflection-point criterion for filament stability (Elhmaidi et al. 2004).

Instability of the submesoscale fronts analyzed in Capet et al. (2008b) is found to be mostly of baroclinic nature, with a dominant  $P_e K_e > 0$  conversion term,

analogous to mixed layer instabilities (MLI) described in Boccaletti et al. (2007). An explanation of this difference is the stronger cross-front velocity shear in the middle of the double jet in the center of the filament compared to a front of comparable width and density magnitude, which makes it easier to meet the criterion for horizontal shear instability.

### b. Potential vorticity injection by winds

The forcing of fronts by downfront winds is known to have an impact on frontogenesis as it induces an additional frontal intensification by the nonlinear cross-frontal Ekman current (Thomas and Lee 2005), and the injection of negative Ertel potential vorticity ( $q < 0$  when  $f > 0$ ) can make the flow symmetrically unstable (Thomas 2005; Thomas et al. 2013). For filaments, with along-axis geostrophic flow in both directions, both signs of  $q$  are injected. The term  $q$  is defined as

$$q = \boldsymbol{\omega}_a \cdot \nabla b, \quad (18)$$

where  $\boldsymbol{\omega}_a = f\mathbf{z} + \nabla \times \mathbf{u}$  is the absolute vorticity vector ( $A$  is its vertical component). The equation for the evolution of  $q$  in its flux form is obtained by taking the curl of the momentum equations and multiplying the result by  $\cdot \nabla b$  and adding it to  $\boldsymbol{\omega}_a \cdot \nabla$  times the buoyancy equation; the result is

$$\frac{\partial q}{\partial t} = -\nabla \cdot \left( q\mathbf{u} - \boldsymbol{\omega}_a \frac{Db}{Dt} + \nabla b \times \mathbf{F} \right). \quad (19)$$

The different terms of the rhs are advection of  $q$  by the flow and creation or destruction of  $q$  both by diabatic processes and by momentum mixing. The vector  $\mathbf{F}$  includes the nonconservative terms of the momentum equations, which when neglecting the horizontal dissipation can be written at the surface:

$$\mathbf{F} \approx \frac{1}{\delta_z} \left( \frac{\tau_{\text{wind}}}{\rho_0} - K_{Mv} \frac{\partial \mathbf{u}}{\partial z} \Big|_{z=-\delta_z} \right),$$

where  $\tau_{\text{wind}}/\rho_0$  is the wind stress ( $\text{m}^2 \text{s}^{-2}$ ), and  $\delta_z$  is the thickness of the first model level. Creation of  $q$  by the wind has the sign of  $-\nabla b \times \tau_{\text{wind}}$  such that the  $q$  injection is negative (positive) when the wind is blowing down-front (upfront); that is, the buoyancy gradient perpendicular to the wind direction is positive (negative).

Maps of  $q$  at the surface and wind stress are in Fig. 17 for filaments  $F_0$  and  $F_1$ . The buoyancy forcing is weak at the time and place of both filaments, and the surface  $q$  flux is controlled by the wind creation and destruction of  $q$ . The orientation of  $F_1$  is perpendicular to the direction of the wind stress, so no  $q$  is created at the surface, and

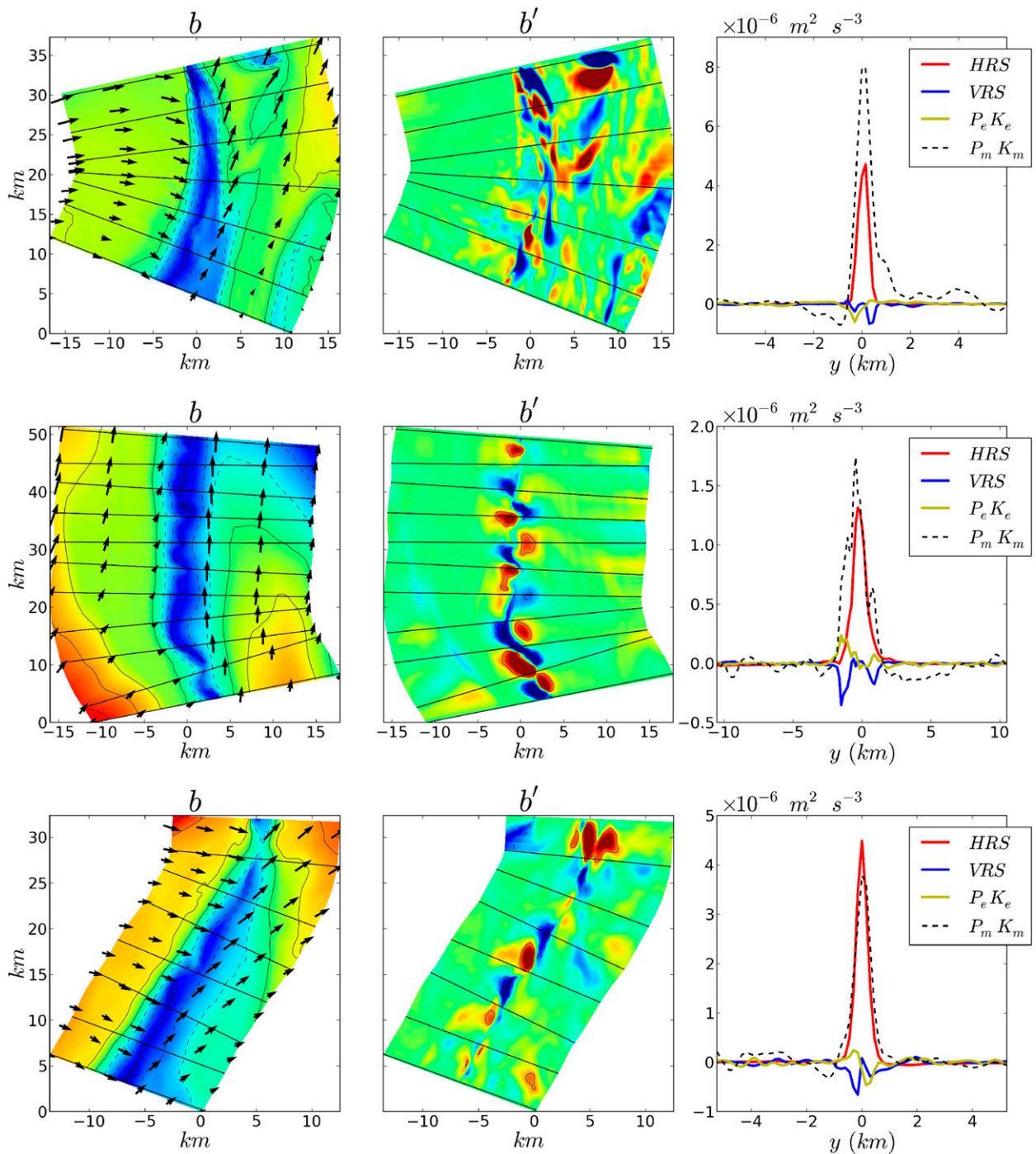


FIG. 16. (left) Total surface buoyancy field  $b$ , (middle) perturbation field  $b'$ , and (right) instantaneous local energy conversions profiles HRS, HRS,  $P_e K_e$ , and  $P_m K_m$  computed for three different unstable cold filaments in their early stages of the instability process: (top)  $F_0$  at the time of Fig. 5c, (middle)  $F_1$ , and (bottom)  $F_2$ .

we see a very small  $q$  signal in Fig. 17. On the other hand,  $F_0$  is favorably aligned with the wind stress, and positive and negative  $q$  are injected in on each side depending on the sign of the buoyancy gradient. The wind is blowing approximately in the negative  $y$  direction (from top to

bottom relative to the upper right panel of Fig. 17), so the left side of the filament has a negative buoyancy gradient along the  $x$  axis, leading to negative  $q$  injection, and the right side of the filament has a positive buoyancy gradient leading to positive  $q$  injection. The positive  $q$

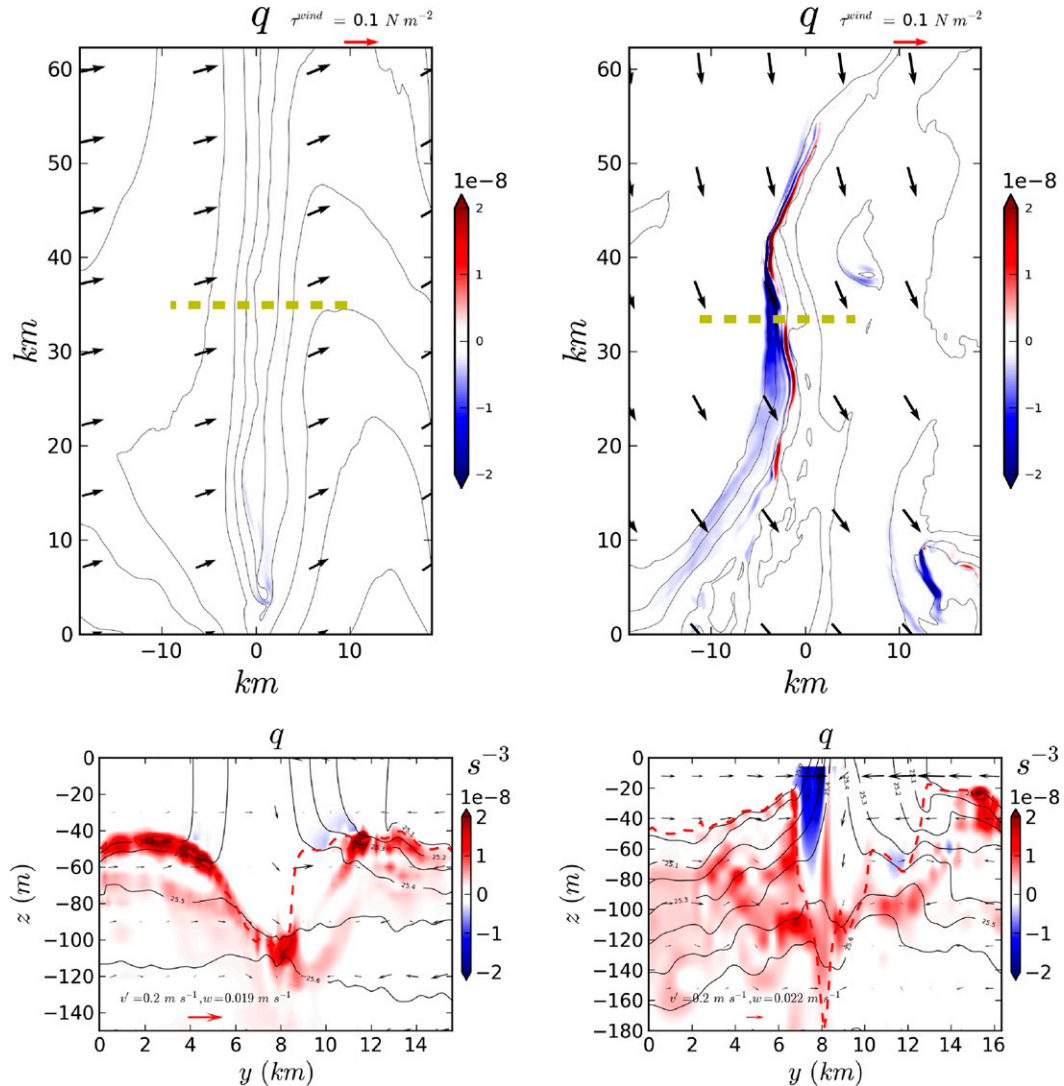


FIG. 17. (top) Instantaneous  $q(x, y)$  in  $s^{-3}$  at the surface during the filamentogenesis for filaments (left)  $F_1$  and (right)  $F_0$ . The black arrows show the direction and magnitude of the wind stress. (bottom) Vertical section of  $q(y, z)$  along the sections indicated by the dashed yellow lines in the corresponding top panels.

stripe is smaller and weaker than the negative one for  $F_0$  as the buoyancy gradient is weaker on the right side (see Fig. 7a).

Vertical sections of potential vorticity are also in Fig. 17 for both filaments. A layer of positive  $q$  is visible at the base of the mixed layer for both filaments due to the large vertical stratification and nonzero vorticity. It is created by vertical buoyancy mixing entraining denser water from the pycnocline into the boundary layer with  $q \approx fb_z$ , and its magnitude is set by the sharpness of the pycnocline there. Filament  $F_1$  has very little  $q$  within the boundary layer itself. In contrast, filament  $F_0$  has large  $q$  there. The upstream side of filament  $F_0$  (i.e., the Gulf Stream is flowing from left to right relative to the  $F_0$  cross section) has a large band of strong negative  $q$  due

to the vortex tilting, that is, strong lateral buoyancy gradient  $b_y$  and vertical alongfront velocity shear  $u_z$ . This negative  $q$  band arises from and is reinforced by the injection of negative  $q$  at the surface due to the wind stress along the filament direction (i.e., directly increasing the vertical velocity shear  $u_z$ ). The impact of the wind is also to further increase the cross-front buoyancy gradient by generating cross-front Ekman currents perpendicular to the wind direction, which participate in reinforcing the ageostrophic secondary circulation of the filament.

The presence of strong negative  $q$  in the flow is a sufficient criterion for the onset of symmetric instability. Even in our highest-resolution simulations, the instability might not be adequately resolved, although in a separating

boundary layer flow with comparable resolution, the  $q < 0$  unstable response is quite evident (Molemaker et al. 2014, manuscript submitted to *J. Phys. Oceanogr.*). However, in this case there is already large mixing prescribed by the KPP parameterization in the region with negative  $q$  even though KPP takes no explicit account of  $q < 0$ , which may act to stabilize the model response. After the wind ceases to inject  $q$  significantly, the boundary layer  $q$  anomaly quickly mixes away within a day, so the response time to symmetric instability is also a consideration.<sup>2</sup> The filament life cycles, and in particular the horizontal shear instability processes (section 6a), are very similar for all the cold filaments considered here. Specifically, filaments  $F_0$  and  $F_1$  behave similarly, even though their wind forcing and  $q$  injections are quite different. Thus, although symmetric instability is likely to occur in favorably forced filaments in nature, its effects do not appear to have a significant impact on the filamentary processes in our simulations.

It should also be noted more generally that, for a strong cold filament close to thermal wind balance in the cross-frontal direction  $y$  ( $fu_z \approx -b_y$ ) with  $f > 0$ , the component of  $q$  due to vortex tilting,  $u_z b_y$ , will always be negative. Considering that the along-filament buoyancy gradients are usually negligible (i.e.,  $-v_z b_x \approx 0$ ), the stratification in the mixed layer has to be large enough so that the vertical component of  $q$  [i.e.,  $(f + \zeta)b_z$ ] dominates or else  $q < 0$  will be a common occurrence.

## 7. Vertical transport and diabatic mixing

Cold filaments are lines of strong oceanic surface convergence with large vertical velocity at their center, which make them potentially a very important contribution to the biogeochemical and physical vertical pumps of the ocean. To illustrate and quantify the role of the submesoscale filaments in generating vertical material fluxes of tracers and in mixing tracer properties, virtual Lagrangian particles can be deployed in the model solutions. Neutrally buoyant particles are advected directly by the model velocity fields without any additional dispersion from the model's mixing processes. Different numerical choices for horizontal and vertical interpolation of the velocity and tracer fields at the position of the particles, as well as different values for the forcing frequency and time step have been used to test the sensitivity of the results without showing significant differences. We use instantaneous outputs every  $\Delta t = 600$  s

from the model to get sufficiently frequent velocity sampling for accurate parcel advection.

A large number of neutrally buoyant particles (i.e.,  $N_{\text{tot}} = 2 \times 10^5$ ) are released in the area surrounding the filament  $F_0$  at a time corresponding to the first panel in Fig. 5. Particles are all released at the same time, uniformly spaced in the first 50 m of the upper ocean, corresponding to the mixed layer depth in this area and season. Figure 18 shows the initial distribution, and the distribution of particles after 30 h, at a latter stage of the filament life cycle, where it has become unstable and is breaking into multiple submesoscale vortices. The horizontal particle trajectories clearly highlight the lines of surface convergence present in the surface flow field. All surface particles are transported within a few hours into these lines that correspond to the filament and part of the adjacent South Wall frontal region. Figure 18 also shows the trajectories of the particles in both density and depth space. The mean depth of the particles goes from  $z = -25$  m, initially, to  $z = -55$  m after a day as a large number of the particles are transported downward at the center of the filament by the filamentary intensification and TTW processes. Particles are transported from the surface to the bottom of the mixed layer at around 100 m and below and are subsequently detrained in the upper thermocline.

About 40% of the particles released in this situation undergo a mixing event during the simulation, defined as a change of density  $\Delta\rho > 0.1 \text{ kg m}^{-3}$ . Partly this is due to surface cooling and boundary layer mixing, but it is especially prevalent near a filament. An example of a typical particle undergoing a diapycnal mixing event through surface cross-filament flow is illustrated in Fig. 19. Density and depth variations following the particle are shown in middle panels. A strong density change ( $\Delta\rho \approx 0.5 \text{ kg m}^{-3}$ ) occurs for the particle over a relatively short period ( $\approx 5$  h) while it is in the upper mixed layer and moves diabatically across the surface density gradient. Following the density change, the particle is adiabatically advected downward from  $z = -20$  m to  $z = -120$  m in about 2 h. The smaller depth variations of the particle later, with an amplitude  $\Delta z \approx 10$  m and a typical period  $T \approx 1$  h, are indications of the abundant internal gravity wave field. The upper panels of Fig. 19 show horizontal and vertical sections of temperature, density, and velocity fields centered on the position of the particle at the instant following the mixing event but prior to downward advection of the particle. The mixing event is associated with the crossing of the upstream side of the filament (from warm to cold, or light to dense) by the particle that is about to reach the center of the filament where it will undergo downward advection. If the filament were adiabatic, then no particles would cross through the

<sup>2</sup> Idealized filament simulations with ROMS with initial  $q < 0$ , with and without vertical mixing (not shown), have a strong symmetric instability response in the latter case but not the former.

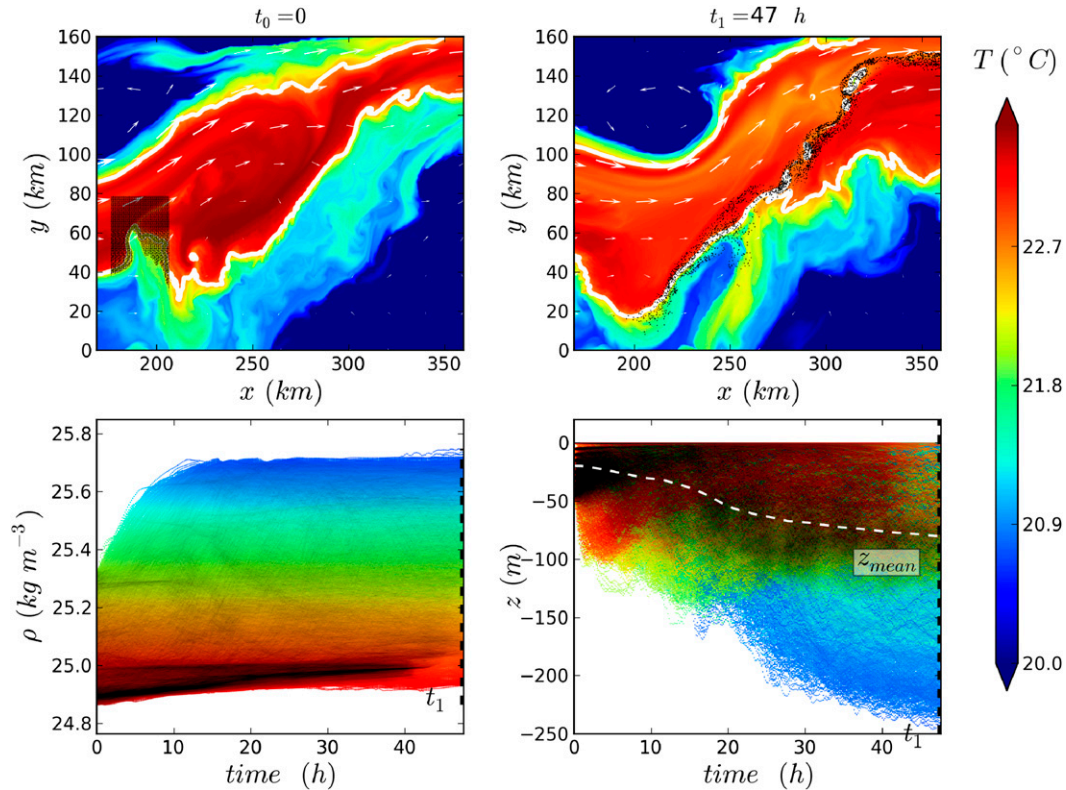


FIG. 18. SST and horizontal position of particles (black dots) at the (top-left) initial time ( $t_0 = 0$ ) and a (top-right) latter stage ( $t_1 = t_0 + 47$  h) for filament  $F_0$  whose life cycle is described in section 3. White vectors show the surface horizontal velocity field and the white contour shows the  $T = 22.4^\circ\text{C}$  isotherm. (bottom-left) Density and (bottom-right) depth evolution of the particles. The dashed white line in the bottom-right panel indicates the mean depth of the particle ensemble. Only 5% of the total number of particles is plotted here.

filament sides, so the boundary layer vertical mixing is essential for this behavior.

Temporal variations of temperature and salinity for a Lagrangian particle in our model are due to either horizontal diffusion or vertical mixing (discounting computational error in a Lagrangian diagnostic applied to an Eulerian model). The vertical mixing [i.e.,  $\partial/\partial z[K_{Tv}(\partial T/\partial z)]$ ] for temperature, where the tracer mixing coefficient  $K_{Tv}$  is computed using the KPP scheme, is plotted in the bottom panels of Fig. 19 in the vertical plane centered at the position of the particle at the same instant. The temperature and salinity variations on both sides of the filament are almost entirely due to the vertical mixing term. The particle plotted in Fig. 19 undergoes a  $\Delta T \approx 1^\circ\text{C}$  temperature variation during a 5-h period. This is consistent with the vertical mixing values of  $\approx -0.5 \times 10^{-4} \text{K s}^{-1}$  at  $z = -20$  m seen in the bottom-left panel of Fig. 19. The horizontal diffusion has a smaller impact, limited to few grid points at the center of the filament where the horizontal velocity shear is the largest (not shown).

The secondary circulation in the cold filament results in advective buoyancy fluxes on both sides of the filament, which act to restratify the flow (i.e.,  $P_m K_m > 0$ ). It brings warm water toward the center of the cold filament at the surface and subsequently expels cold water from the center of the filament at the base of the boundary layer. These effects are partly compensated by the vertical mixing that mixes the warmer water at the surface with the colder water at the bottom of the mixed layer.

Figure 19 also shows the corresponding vertical section for potential vorticity  $q$ , which exhibits the same structure as seen previously for  $F_0$  in Fig. 17, with injection of  $q$  at the surface due to the wind stress along the filament direction. The large density variations along the trajectory have accompanying large diabatic  $q$  changes (not shown) as the particle moves through the strong negative  $q$  region in the mixed layer.

## 8. Summary and conclusions

Insights from theory, observations, and realistic, high-resolution simulations show that buoyancy filaments are

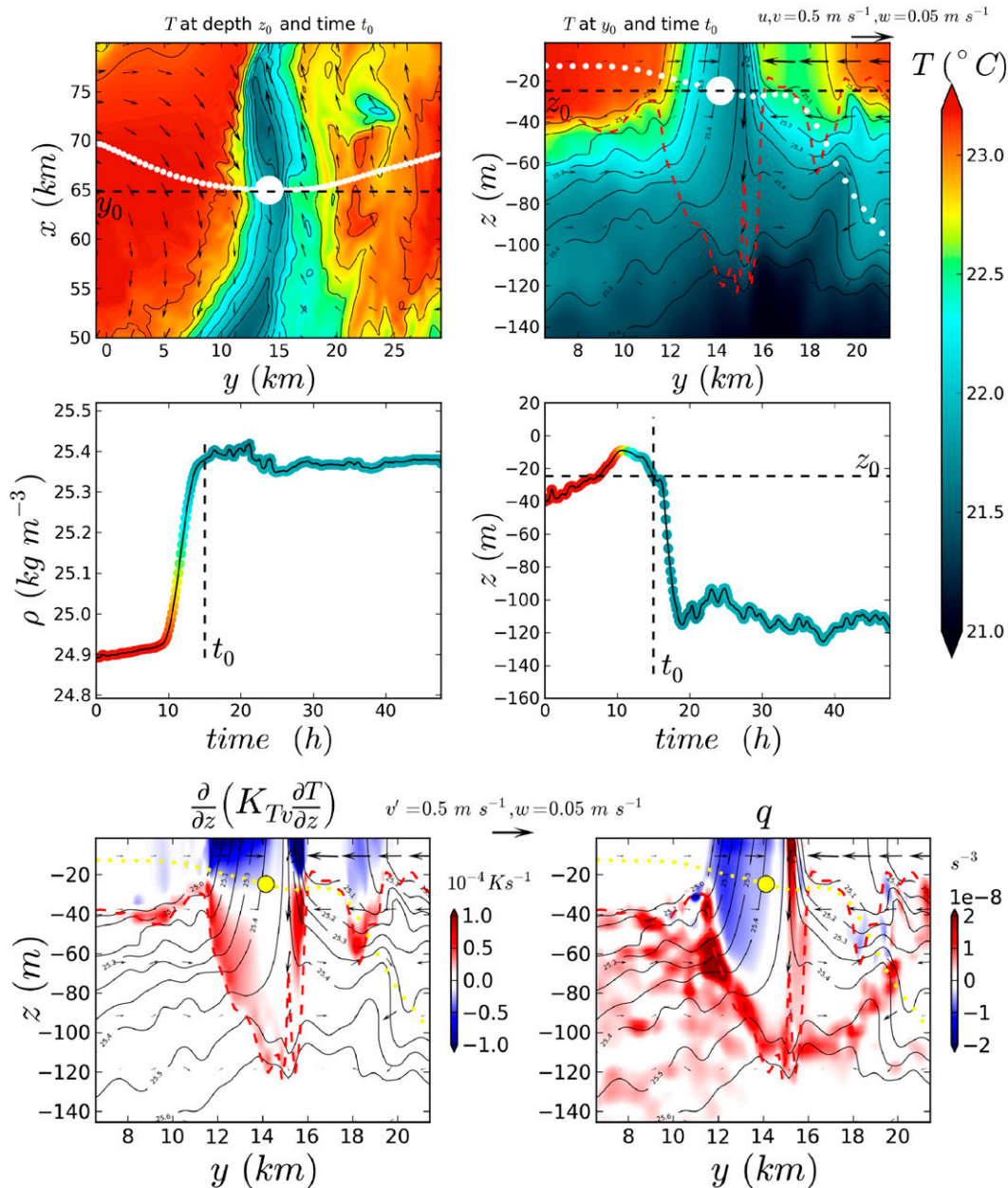


FIG. 19. Temperature (K, colors), density anomaly  $\text{kg m}^{-3}$ , black contours), and velocity ( $\text{m s}^{-1}$ , vectors) in the (top-left) horizontal and (top-right) vertical planes centered on the position of one Lagrangian particle (marked as a white dot) inside filament  $F_0$  at a time  $t = t_0$ . Smaller white dots show the past and future position of the particle. (middle-left) Density and (middle-right) depth evolution of the particle. Colored dots show the temperature of the particle at the corresponding position using the same colorscale as in the upper panels. (bottom-left) Instantaneous vertical temperature mixing term  $\partial/\partial z[K_T v(\partial T/\partial z)]$  ( $\text{K s}^{-1}$ ) and (bottom-right) potential vorticity  $q$  ( $\text{s}^{-3}$ ).

numerous in nature and dynamically active. They are conspicuously abundant on the subtropical gyre interior side of the Gulf Stream. In this paper, different examples of such intense submesoscale cold filaments are presented and analyzed using a set of realistic very high-resolution simulations. The life cycle of the filaments includes their formation and intensification through

filamentogenesis and ultimately the arrest of filamentogenesis and filament destruction by submesoscale instabilities.

The filamentogenesis is primarily due to horizontal straining flows with a strong positive signal in the middle of the filament. Vertical mixing opposes the frontogenetic effect of the advection with a negative signal at the

center, but has a positive signal on the exterior sides of the filaments. Vertical straining weakens the fronts everywhere but is significant only at depth. Horizontal diffusion also weakens the front; it is largest at the surface where the velocity shear is also maximum, but it is not a dominant effect in our simulated filaments. Filamentary intensification can be understood as a dual frontogenetic process, along the lines described in the results for single fronts in [Capet et al. \(2008b\)](#). There is, however, a stronger asymmetry of the vertical velocity due to the amplification at the center of the filament.

A classical thermal wind balance is often not adequate to describe these filaments. The effect of the vertical mixing of momentum due to turbulence in the surface layer is of the same order of importance as the pressure gradient and Coriolis forces in a turbulent thermal wind balance (TTW). Solving this TTW balance provides a very reliable estimate of the ageostrophic secondary circulation sharpening the filament and of the corresponding vertical velocity in the surface layer. Thus, after the initial intensification of filaments by the ambient strain field, a sustained filamentogenesis can ensue even if the strain abates, where the secondary circulation is due to TTW.

For the cold filaments that were studied in this paper, the process of filamentogenesis is arrested by vigorous submesoscale instabilities. The energy source for these unstable perturbations is the horizontal Reynolds stress, transferring energy from the strong shear in the cross-filament direction to the growing perturbations. This is different from the frontal cases discussed in [Capet et al. \(2008b\)](#), where baroclinic conversion is the primary cause of the frontal instabilities. However, it is similar to the submesoscale instabilities that were studied in [Molemaker et al. \(2010\)](#). The difference in flow regimes where either baroclinic conversion or barotropic shear conversion are dominant appears to be mostly a matter of horizontal scales. At larger submesoscales, instabilities are predominantly driven by release of potential energy through baroclinic conversion. At smaller horizontal scales, the horizontal shear grows until the dominant energy source is through horizontal Reynolds stress and barotropic shear conversion. In our case, the sharpening of the fronts that form the filaments is amplified by filamentogenesis such that they reach scales at which the horizontal shear instability is predominant despite the competition with the mixed layer baroclinic instability.

Injection of  $q$  by the wind is visibly present in our simulations but does not appear to be essential to the filament life cycles. Negative  $q$  is a condition for the onset of symmetric instability, which may not be well resolved even at the highest resolution here ( $\Delta x = 150$  m). However, we observe in regions with negative  $q$ ,

where symmetric instability is indicated, that vertical mixing is strong and mixes away the injected  $q$  anomaly within a day or so.

The filaments are lines of strong oceanic surface convergence as illustrated by the release of Lagrangian particles near the surface of the Gulf Stream. Diabatic mixing is strong as particles move across the filament edge in the mixed layer. The vertical mixing due to turbulence in the surface layer allows particles to horizontally cross the density gradients. Once particles have reached the center of the filament, they downwell adiabatically and move away within the pycnocline. A significant part of the particles initially present in the surface layer in the vicinity of the forming filament are transported vertically during the filamentogenesis process. This highlights the important role played by such submesoscale structures as sources of tracer injection.

The dynamics in the mixed layer are strongly influenced by the KPP parameterization, which treats a variety of unresolved processes involved in vertical mixing ([Large et al. 1994](#)). It has been extensively compared to large eddy simulations, in situ measurements, and observations ([Large et al. 1997](#); [Large and Gent 1999](#)) and is used in a majority of ocean circulation models. However, the spatial and time scales involved in the processes presented here are at the edge of the scales for which the KPP parameterization was originally designed and has been extensively tested. Submesoscale and subinertial time-scale dynamics in the heterogeneous environments of fronts and filaments could potentially impact the validity of KPP, which would either over- or underestimate the level of vertical mixing, as noted by [Inoue et al. \(2010\)](#). Numerical studies using large eddy simulations could be used to further investigate the validity of mixed layer parameterizations in the presence of lateral gradients and short time scales.

The process of filamentogenesis creates horizontally localized regions [ $O(1)$  km] in which the magnitude of the vertical velocity becomes large, as illustrated by [Fig. 6](#). The hydrostatic approximation might be less valid in these regions. It is, however, not possible to directly quantify nonhydrostatic effects in a hydrostatic model. [Mahadevan \(2006\)](#) performed comparisons of hydrostatic and nonhydrostatic simulations for submesoscale processes at ocean fronts in a comparable flow regime with horizontal resolutions up to  $\Delta x = 250$  m without being able to identify categorical differences. [Molemaker et al. \(2010\)](#) have evaluated the departure from hydrostatic balance using a Boussinesq model and also found that the error in hydrostatic balance remains small in most places. The degree to which nonhydrostatic effects will impact filamentogenesis at these scales is probably small but is currently unquantified.

The filament examples presented here happen during late winter conditions for the Gulf Stream. Although similar types of filaments can be found at all times throughout the year, seasonal variations are usually significant for submesoscale fronts and filaments, especially in the Gulf Stream region (Mensa et al. 2013). The depth of the mixed layer controls the reservoir of available potential energy that is a primary source for submesoscale generation through mixed layer instability. Mixed layer variations are mostly driven by atmospheric forcing that has a strong seasonality. Winter cooling of the ocean by the atmosphere acts to increase mixing, mixed layer depth, and submesoscale activity, while summer heating acts to restratify the surface layer of the ocean, causing a reduction of the mixed layer depth and of the submesoscale activity. This is, however, mostly true in the submesoscale soup, away from the strong mean currents. The Gulf Stream itself is less sensitive to surface forcing. The mixed layer depth  $h_{ml}$  in the core of the Gulf Stream varies between  $20\text{ m} < h_{ml} < 60\text{ m}$ , depending on the season while the amplitude of the variations away from the Gulf Stream are much bigger ( $0\text{ m} < h_{ml} < 300\text{ m}$ ). Available potential energy is also not the only source of energy for the formation of the intense fronts and filaments on both sides of the Gulf Stream; they are created by the mean current gradients and mesoscale turbulence, for which seasonality is not as predominant (e.g., Zhai et al. 2008).

Most of the results presented here in the context of submesoscale cold filaments on the South Wall of the Gulf Stream are expected to be valid for a much wider range of filamentary and frontal structures. The filamentogenesis process is generic, and conclusions drawn here should apply as well to the weaker filaments in open-ocean submesoscale turbulence. Idealized studies are needed to confirm the generality and further refine the theoretical understanding of a number of aspects of filamentary dynamics. The predominance of the TTW balance is expected to be valid for most submesoscale flows in the presence of a turbulent mixed layer. Future work can assess the accuracy of the TTW balance and better diagnose boundary layer turbulence and vertical velocities around fronts, filaments, and surface-layer vortices.

*Acknowledgments.* We appreciate support from the Office of Naval Research (N00014-12-1-0939 and N00014-12-1-0105) and the National Science Foundation (OCE-1049134).

#### REFERENCES

- Barnier, B., L. Siefried, and P. Marchesiello, 1995: Thermal forcing for a global ocean circulation model using a three-year climatology of ECMWF analyses. *J. Mar. Syst.*, **6**, 363–380, doi:10.1016/0924-7963(94)00034-9.
- Beckmann, A., and D. Haidvogel, 1993: Numerical simulation of flow around a tall isolated seamount. Part I: Problem formulation and model accuracy. *J. Phys. Oceanogr.*, **23**, 1736–1753, doi:10.1175/1520-0485(1993)023<1736:NSOFAA>2.0.CO;2.
- Boccaletti, G., R. Ferrari, and B. Fox-Kemper, 2007: Mixed layer instabilities and restratification. *J. Phys. Oceanogr.*, **37**, 2228–2250, doi:10.1175/JPO3101.1.
- Capet, X., J. McWilliams, M. Molemaker, and A. Shchepetkin, 2008a: Mesoscale to submesoscale transition in the California Current System. Part I: Flow structure, eddy flux, and observational tests. *J. Phys. Oceanogr.*, **38**, 29–43, doi:10.1175/2007JPO3671.1.
- , —, —, and —, 2008b: Mesoscale to submesoscale transition in the California Current System. Part II: Frontal processes. *J. Phys. Oceanogr.*, **38**, 44–64, doi:10.1175/2007JPO3672.1.
- Carton, J., and B. Giese, 2008: A reanalysis of ocean climate using Simple Ocean Data Assimilation (SODA). *Mon. Wea. Rev.*, **136**, 2999–3017, doi:10.1175/2007MWR1978.1.
- Conkright, M., R. Locarnini, H. Garcia, T. O'Brien, T. Boyer, C. Stephens, and J. Antonov, 2002: *World Ocean Atlas 2001: Objective Analyses, Data Statistics and Figures*. National Oceanographic Center Internal Tech. Rep. 17, CD-ROM.
- Dritschel, D., P. Haynes, M. Jukes, and T. Shepherd, 1991: The stability of a two-dimensional vorticity filament under uniform strain. *J. Fluid Mech.*, **230**, 647–665, doi:10.1017/S0022112091000915.
- Elhmaidi, D., A. Provenzale, T. Lili, and A. Babiano, 2004: Stability of two-dimensional vorticity filaments. *Phys. Lett.*, **333A**, 85–90, doi:10.1016/j.physleta.2004.10.033.
- Garrett, C., and J. Loder, 1981: Dynamical aspects of shallow sea fronts. *Philos. Trans. Roy. Soc. London*, **B302**, 563–581, doi:10.1098/rsta.1981.0183.
- Harvey, B., and M. Ambaum, 2010: Instability of surface-temperature filaments in strain and shear. *Quart. J. Roy. Meteor. Soc.*, **136**, 1506–1513, doi:10.1002/qj.651.
- Held, I., R. Pierrehumbert, S. Garner, and K. Swanson, 1995: Surface quasi-geostrophic dynamics. *J. Fluid Mech.*, **282**, 1–20, doi:10.1017/S0022112095000012.
- Holland, W., J. Chow, and F. Bryan, 1998: Application of a third-order upwind scheme in the NCAR ocean model. *J. Climate*, **11**, 1487–1493, doi:10.1175/1520-0442(1998)011<1487:AOATOU>2.0.CO;2.
- Holton, J., 1982: The role of gravity wave induced drag and diffusion in the momentum budget of the mesosphere. *J. Atmos. Sci.*, **39**, 791–799, doi:10.1175/1520-0469(1982)039<0791:TROGWI>2.0.CO;2.
- Inoue, R., R. Harcourt, and M. Gregg, 2010: Mixing rates across the Gulf Stream, Part 2: Implications for nonlocal parameterization of vertical fluxes in the surface boundary layers. *J. Mar. Res.*, **68**, 673–698, doi:10.1357/002224011795977626.
- Jukes, M., 1995: Instability of surface and upper-tropospheric shear lines. *J. Atmos. Sci.*, **52**, 3247–3262, doi:10.1175/1520-0469(1995)052<3247:IOSAUT>2.0.CO;2.
- Lapeyre, G., and P. Klein, 2006: Impact of the small-scale elongated filaments on the oceanic vertical pump. *J. Mar. Res.*, **64**, 835–851, doi:10.1357/002224006779698369.
- Large, W., and P. Gent, 1999: Validation of vertical mixing in an equatorial ocean model using large eddy simulations and observations. *J. Phys. Oceanogr.*, **29**, 449–464, doi:10.1175/1520-0485(1999)029<0449:VOVMIA>2.0.CO;2.

Barnier, B., L. Siefried, and P. Marchesiello, 1995: Thermal forcing for a global ocean circulation model using a three-year

- , J. M. Williams, and S. Doney, 1994: Oceanic vertical mixing: A review and a model with a nonlocal boundary layer parameterization. *Rev. Geophys.*, **32**, 363–403, doi:10.1029/94RG01872.
- , G. Danabasoglu, S. Doney, and J. M. Williams, 1997: Sensitivity to surface forcing and boundary layer mixing in a global ocean model: Annual-mean climatology. *J. Phys. Oceanogr.*, **27**, 2418–2447, doi:10.1175/1520-0485(1997)027<2418:STSFAB>2.0.CO;2.
- Lee, T., J. Yoder, and L. Atkinson, 1991: Gulf Stream frontal eddy influence on productivity of the southeast U.S. continental shelf. *J. Geophys. Res.*, **96**, 22 191–22 205, doi:10.1029/91JC02450.
- Lehahn, Y., F. d’Ovidio, M. Lévy, and E. Heifetz, 2007: Stirring of the northeast Atlantic spring bloom: A Lagrangian analysis based on multisatellite data. *J. Geophys. Res.*, **112**, C08005, doi:10.1029/2006JC003927.
- Lemarié, F., J. Kurian, A. Shchepetkin, M. Molemaker, F. Colas, and J. McWilliams, 2012: Are there inescapable issues prohibiting the use of terrain-following coordinates in climate models? *Ocean Modell.*, **42**, 57–79, doi:10.1016/j.ocemod.2011.11.007.
- Mahadevan, A., 2006: Modeling vertical motion at ocean fronts: Are nonhydrostatic effects relevant at submesoscales? *Ocean Modell.*, **14**, 222–240, doi:10.1016/j.ocemod.2006.05.005.
- , and A. Tandon, 2006: An analysis of mechanisms for submesoscale vertical motion at ocean fronts. *Ocean Modell.*, **14**, 241–256, doi:10.1016/j.ocemod.2006.05.006.
- Marchesiello, P., J. McWilliams, and A. Shchepetkin, 2001: Open boundary conditions for long-term integration of regional oceanic models. *Ocean Modell.*, **3**, 1–20, doi:10.1016/S1463-5003(00)00013-5.
- Mason, E., M. Molemaker, A. Shchepetkin, F. Colas, J. McWilliams, and P. Sangra, 2010: Procedures for offline grid nesting in regional ocean models. *Ocean Modell.*, **35**, 1–15, doi:10.1016/j.ocemod.2010.05.007.
- McWilliams, J., and M. Molemaker, 2011: Baroclinic frontal arrest: A sequel to unstable frontogenesis. *J. Phys. Oceanogr.*, **41**, 601–619, doi:10.1175/2010JPO4493.1.
- , I. Yavneh, M. Cullen, and P. Gent, 1998: The breakdown of large-scale flows in rotating, stratified fluids. *Phys. Fluids*, **10**, 3178–3184, doi:10.1063/1.869844.
- , F. Colas, and M. Molemaker, 2009a: Cold filamentary intensification and oceanic surface convergence lines. *Geophys. Res. Lett.*, **36**, L18602, doi:10.1029/2009GL039402.
- , M. Molemaker, and E. Olafsdottir, 2009b: Linear fluctuation growth during frontogenesis. *J. Phys. Oceanogr.*, **39**, 3111–3129, doi:10.1175/2009JPO4186.1.
- Mensa, J., Z. Garraffo, A. Griffa, T. Ozgokmen, A. Haza, and M. Veneziani, 2013: Seasonality of the submesoscale dynamics in the Gulf Stream region. *Ocean Dyn.*, **63**, 923–941, doi:10.1007/s10236-013-0633-1.
- Molemaker, M., J. McWilliams, and X. Capet, 2010: Balanced and unbalanced routes to dissipation in an equilibrated Eady flow. *J. Fluid Mech.*, **654**, 35–63, doi:10.1017/S0022112009993272.
- Penven, P., L. Debreu, P. Marchesiello, and J. McWilliams, 2006: Application of the ROMS embedding procedure for the central California upwelling system. *Ocean Modell.*, **12**, 157–187, doi:10.1016/j.ocemod.2005.05.002.
- Plougonven, R., and C. Snyder, 2007: Inertia-gravity waves spontaneously generated by jets and fronts. Part I: Different baroclinic life cycles. *J. Atmos. Sci.*, **64**, 2502–2520, doi:10.1175/JAS3953.1.
- Ponte, A., P. Klein, X. Capet, P.-Y. Le Traon, B. Chapron, and P. Lherminier, 2013: Diagnosing surface mixed layer dynamics from high-resolution satellite observations: Numerical insights. *J. Phys. Oceanogr.*, **43**, 1345–1355, doi:10.1175/JPO-D-12-0136.1.
- Risien, C., and D. Chelton, 2008: A global climatology of surface wind and wind stress fields from eight years of QuikSCAT scatterometer data. *J. Phys. Oceanogr.*, **38**, 2379–2413, doi:10.1175/2008JPO3881.1.
- Roulet, G., and P. Klein, 2010: Cyclone-anticyclone asymmetry in geophysical turbulence. *Phys. Rev. Lett.*, **104**, 218501, doi:10.1103/PhysRevLett.104.218501.
- Shchepetkin, A., and J. McWilliams, 2005: The Regional Oceanic Modeling System (ROMS): A split-explicit, free-surface, topography-following-coordinate ocean model. *Ocean Modell.*, **9**, 347–404, doi:10.1016/j.ocemod.2004.08.002.
- , and —, 2008: Computational kernel algorithms for fine-scale, multiprocess, longtime oceanic simulations. *Handb. Numer. Anal.*, **14**, 121–183, doi:10.1016/S1570-8659(08)01202-0.
- , and —, 2011: Accurate Boussinesq modeling with a practical, “stiffened” equation of state. *Ocean Modell.*, **38**, 41–70, doi:10.1016/j.ocemod.2011.01.010.
- Shcherbina, A., E. D’Asaro, C. Lee, J. Klymak, M. Molemaker, and J. McWilliams, 2013: Statistics of vertical vorticity, divergence, and strain in a developed submesoscale turbulence field. *Geophys. Res. Lett.*, **40**, 4706–4711, doi:10.1002/grl.50919.
- Silva, A. D., C. Young, and S. Levitus, 1994: *Algorithms and Procedures*. Vol. 1, *Atlas of Surface Marine Data 1994*, NOAA Atlas NESDIS 6, 74 pp.
- Smith, W., and D. Sandwell, 1997: Global seafloor topography from satellite altimetry and ship depth soundings. *Science*, **277**, 1957–1962, doi:10.1126/science.277.5334.1956.
- Thomas, L., 2005: Destruction of potential vorticity by winds. *J. Phys. Oceanogr.*, **35**, 2457–2466, doi:10.1175/JPO2830.1.
- , and C. Lee, 2005: Intensification of ocean fronts by down-front winds. *J. Phys. Oceanogr.*, **35**, 1086–1102, doi:10.1175/JPO2737.1.
- , J. Taylor, R. Ferrari, and T. Joyce, 2013: Symmetric instability in the Gulf Stream. *Deep-Sea Res.*, **91**, 96–110, doi:10.1016/j.dsr2.2013.02.025.
- Webb, D., B. de Cuevas, and C. Richmond, 1998: Improved advection schemes for ocean models. *J. Atmos. Oceanic Technol.*, **15**, 1171–1187, doi:10.1175/1520-0426(1998)015<1171:IASFOM>2.0.CO;2.
- Zhai, X., R. Greatbatch, and J.-D. Kohlmann, 2008: On the seasonal variability of eddy kinetic energy in the Gulf Stream region. *Geophys. Res. Lett.*, **35**, L24609, doi:10.1029/2008GL036412.